Biogeosciences

Open Access EGU

The Volyn biota (Ukraine) – indications of 1.5 Gyr old eukaryotes in 3D preservation, a spotlight on the "boring billion"

Gerhard Franz[1], Vladimir Khomenko[1,2], Peter Lyckberg[3], Vsevolod Chournousenko[4], Ulrich Struck[5],
Ulrich Gernert[6], and Jörg Nissen[6]

[1]Institut für Angewandte Geowissenschaften, Technische Universität Berlin, 10587 Berlin, Germany
[2]M.P. Semenenko Institute of Geochemistry, Mineralogy and Ore Formation, The National Academy of Sciences of Ukraine,
34 Palladina ave., Kyiv, 03142, Ukraine
[3]Luxembourg National Museum of Natural History, 25 Rue Münster, 2160 Luxembourg, Luxembourg
[4]Volyn Quartz Samotsvety Company, Khoroshiv (Volodarsk-Volynski), Ukraine
[5]Museum für Naturkunde, Leibniz-Institut für Evolutions- und Biodiversitätsforschung,
Invalidenstraße 43, 10115 Berlin, Germany
[6]Zentraleinrichtung Elektronenmikroskopie, Technische Universität Berlin, 10623 Berlin, Germany

Correspondence: Gerhard Franz (gefra548@gmail.com, gerhard.franz@tu-berlin.de)

Abstract. The Volyn biota, fossilized organisms with a minimum age of 1.5 Ga, were found in cavities in granitic pegmatites from the Korosten Pluton, NW Ukrainian shield. Fossilization was due to an influx of hydrothermal fluorine-rich waters, which silicified the outermost part of the organisms, thus preserving the 3D morphology. Details of the morphology (investigated by scanning electron microscopy) show that the majority of the specimens are filamentous, of a large variety with diameters ranging from ~ 10 to $\sim 200\,\mu\text{m}$, thin filaments with typical branching and thick filaments with ball-shaped outgrowths and dented surface. Filaments can be straight or conical, curvilinear, or strongly curved, up to millimeters in length, some with a central channel. Some filaments show indications of segmentation and are grown as sessile organisms onto substrate; others show both intact ends, indicating a non-sessile, free-living lifestyle. Objects with flaky morphology and agglutinating filaments are interpreted as fossil biofilms. Other objects are hollow and show a large variety of forms; spherical objects are scarce. Infrared spectroscopy indicates the presence of chitosan in one filament type, electron microprobe analysis of nanometer-sized inclusions in filaments identified the presence of Bi(Te,S) minerals, and both observations are compatible with the interpretation as fungi-like organisms. Stable C- and N-isotope data of bulk samples are in the range of $-31\,‰$ to $-47\,‰$

$\delta^{13}\text{C}$ and of $+3\,‰$ to $+10\,‰$ $\delta^{15}\text{N}$, indicating possible methanogens as part of the subsurface microecosystem. The Volyn biota indicate that at 1.5 Ga complex forms of life existed in the continental deep biosphere, well above the microscopic level, including fungi-like organisms resembling eukaryotes.

1 Introduction

Precambrian fossils are generally not well preserved because of the absence of skeletal parts. In addition, most Precambrian fossil record is from sedimentary rocks with strong diagenetic or even metamorphic overprint, which destroyed much of the original morphology and in extreme cases of very old organisms left only an isotopic signature (e.g., Alleon et al., 2018; Berbee et al., 2020). Therefore, their biogenicity is often disputed especially when the organic matter (OM) is completely replaced, often by silica or pyrite. A preservation of 3D morphology is very rare and requires special fossilization conditions, which include first prevention of rapid decay of the OM and then preservation of the space around the fossil in order to preserve its original morphology. These conditions were fulfilled in pegmatites of the Volyn pegmatite field, Ukraine,

associated with the Korosten Pluton. These so-called "chamber pegmatites" contain large miarolitic cavities in which OM named (oxy)-kerite was found and in previous investigations interpreted as an example of abiogenic formation (Ginzburg et al., 1987; Luk'yanova et al., 1992), later re-interpreted as fossil cyanobacteria (Gorlenko et al., 2000; Zhmur, 2003) from a geyser type deposit. Ginzburg et al. (1987) give a composition of 60 wt %–76 wt % C, 5 wt %–7 wt % H, 9 wt %–23 wt % O, 8 wt %–9 wt % N, and 2 wt %–3 wt % S and an empirical formula of $C_{491}H_{386}O_{87}(S)N$. Gorlenko et al. (2000) and Zhmur (2003) mention masses of up to 3 kg of kerite in one of the cavities with an irregular distribution within the pegmatite.

The organisms lived in these cavities and provide an example of the Precambrian deep biosphere. Their fossilization conditions included sudden influx of hot hydrothermal waters in the geyser system, where magmatic fluids rich in SiF_4 mixed with meteoric waters (Franz et al., 2022a), infiltration of Si–Al into the outermost layer of the fossils, and formation of dominantly clay mineral encrustations. The 1.76 Ga intrusion age of the pegmatites (U–Pb zircon; Shumlyanskyy et al., 2021) provides a maximum age of the fossils; the minimum age of 1.5 Ga is provided by the age of formation of a breccia, which contains degraded OM, brown opal with OM, buddingtonite whose NH_4 content was provided by the degraded OM, and muscovite (^{40}Ar–^{39}Ar laser ablation data; Franz et al., 2022b). An additional argument for this age comes from the brown opal, which cements the breccia and contains organic matter (Franz et al., 2017, and references therein). Therefore, we assume that breccia formation must have occurred when organic matter was already present in the "chambers". Although some of the miarolitic chambers collapsed, producing the muscovite–opal-bearing breccia, other chambers are still intact and have been mined since the 1930s for piezo quartz and until now for pegmatite minerals such as beryl and topaz (Ivanovich and Alekseevich, 2007; Lyckberg et al., 2009, 2019).

We report here details about the morphology and the internal structure of the fossils, investigated by scanning electron microscopy (SEM) and electron microprobe analysis (EMPA), and provide stable C–N isotope and infrared spectroscopy (FTIR) data, which allow speculating about the types of organisms. An important point is that these "micro"-fossils in many cases reach a size well above the microscopic level, with filaments of several millimetres in length. The age of the fossils is 1.5 Ga in the middle of the "boring billion" and gives insight into the organisms of the deep continental biosphere.

2 Geological framework and sample material

The locality in the Ukrainian Precambrian shield is associated with the Korosten anorthosite–mangerite–charnockite–granite plutonic complex (Shumlyanksyy et al., 2012)

(Fig. 1). The samples were recovered from underground in shaft 3 of the mine from a depth of approximately 100 m. One sample was obtained from the mineralogical museum of the Academy of Sciences, Kyiv, and one beryl sample with kerite on beryl was collected from the mine tailings (Table 1). Two additional samples of topaz from the museum in Kyiv with kerite (Fig. 2) were not investigated in detail. The samples from underground could be simply picked up with no need for separation from rock matrix and were stored in plastic sample bags. Kerite has not been found outside the cavities, which are in the core of the pegmatite. It exists as fine fiber masses between fragments of the wall of the cavities and as larger masses hanging freely on the walls, attached to feldspar and often around topaz (Fig. 2b, c) and to beryl (Fig. 2d–j). The bottom of the cavities is covered with soft clay.

Sample no. 0 consists of broken filaments of several millimeters in length (Fig. 2a), and it is likely that the original length was much larger on the centimeter scale. On beryl it was found attached to dissolution features on the surface of the crystals, but not only in the common filamentous form, but also in irregular shape (Fig. 2d–j) and rarely in spherical shape (Fig. 2i). Although the previous reports mention mostly filaments with smooth surface, our new observations revealed a large variety of different types of filaments, described below.

3 Methods

The samples were investigated by SEM and EMPA. SEM images were obtained with a Hitachi SU8030 instrument, equipped with an EDAX EDS system with a 30 mm^2 silicon drift detector (SDD) fitted with a silicon nitride window. Samples were coated with an approximately 5 nm thick Ir layer allowing for high-resolution imaging of the filaments' surfaces without the structure of commonly applied Au coating. The kerite samples without further cleaning or preparation were mounted on Al stubs stickered with conductive carbon tabs. The beryl crystals with kerite filaments were dust-cleaned with compressed air and coated with C.

The JEOL JXA-8530F field emission electron microprobe at TU Berlin was used to investigate mounts embedded in epoxy, but with C-coating, for quantitative results and less absorbance (compared to Ir). EMPA data for element distribution maps of cross sections or of parts of the rim of the filaments and flaky kerite were acquired in the wavelength dispersive mode using an 8 kV, 20 nA beam with a probe diameter of 64 nm. Back-scattered electron (BSE) images were taken to select appropriate sites. Mappings were done in stage scan modus with pixel resolution between 277 and 360 × 180 and 265, with a pixel size of mostly 80 nm, and a dwell time per pixel of 200 ms. Total scan areas varied between 70 × 36 and 33.2 × 31.8 µm.
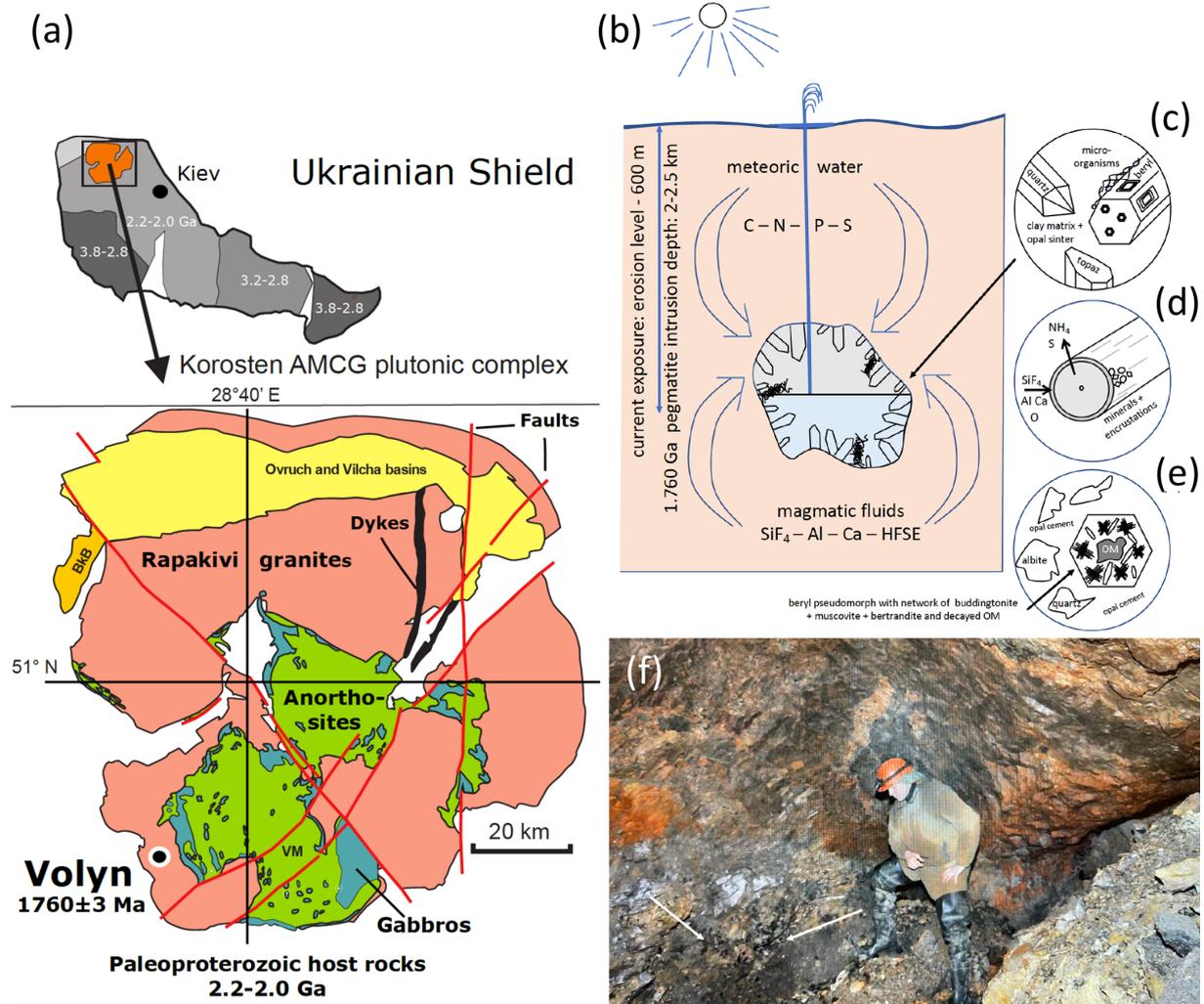
Figure 1. (a) Location of the Volyn pegmatite field in the Ukrainian shield, which hosts the Volyn biota, and sketch map of the Korosten Pluton. (b) Conceptual model for the fossilization in the miarolitic cavities ("chambers") in the pegmatite. Current exposure is from the erosion level to a depth of 600 m. Kerite is attached to the walls, often to feldspar, but also (c) on topaz and beryl crystals. (d) Fossilization produces a thin rim of Si–Al enrichment and encrustations of clay minerals. (e) In collapsed chambers, a breccia formed with pseudomorph of buddingtonite + muscovite + opal after beryl. Decaying kerite produced NH_4 for formation of buddingtonite. The 1.5 Ga Ar–Ar age of muscovite is considered the minimum age for the fossils. (f) View into a chamber, arrows point to black kerite (all images reproduced from Franz et al., 2022a).

Table 1. List of samples.

| No./German Research Centre for Geosciences (GFZ) no.	Year of sampling	Material	Location
0/Museum Ac. Sci. Kyiv	unknown	kerite	unknown
1/G017809	2018	kerite	shaft 3
2/G017810	2018	kerite	shaft 3
3/G017811	2018	kerite	shaft 3
4/G017812	2018	kerite	shaft 3
5/G017813	2013	kerite	shaft 3
6/G017814	2013	kerite	shaft 3
7/G017815	2013	kerite	shaft 3
2008-V-10	2008	beryl crystal with etch pits	mine tailings pegmatite no. 2
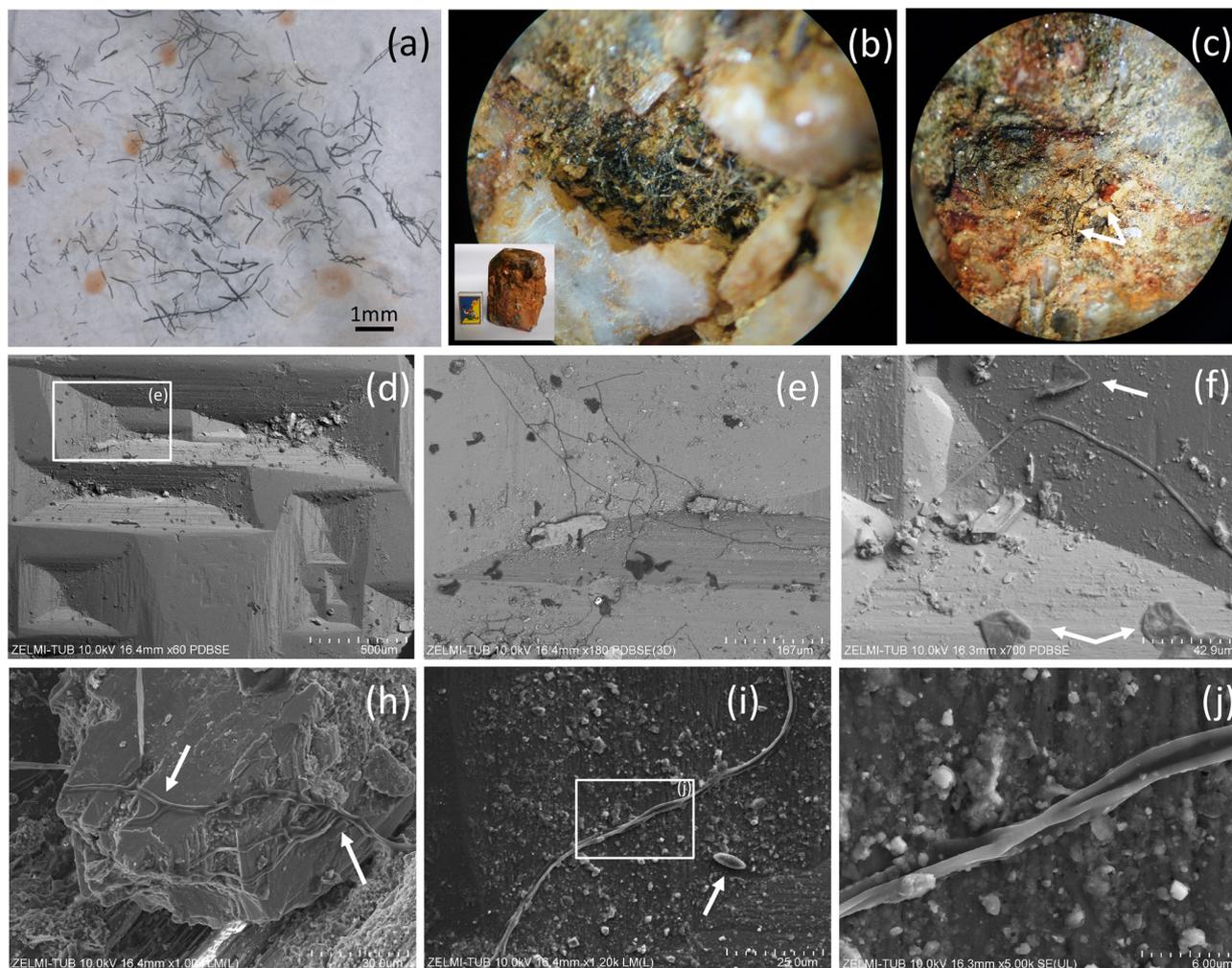
Figure 2. (a) Photograph of sample no. 0, illustrating the pieces of broken, solitary kerite filaments of millimeter length. **(b)** Photograph of kerite filaments on topaz (white crystals with iron oxide hydroxide staining; inset shows topaz crystal with 5 cm large matchbox for scale, image diameter approximately 2 mm). **(c)** Filaments of different diameter on topaz (arrows; image diameter approximately 3 mm). **(d)** SEM image (with combined back scattered mode) of beryl prism surface with characteristic etch pits. Rectangle indicates position of **(e)**, which shows filamentous kerite together with kerite in irregular shape (dark contrast indicates organic matter). **(f)** SEM image, arrows point to kerite with irregular shape. **(h)** Kerite filaments with branching (arrows) in dissolution feature of beryl. **(i)** Kerite filament and spherical kerite (arrow) in an etch pit of beryl; rectangle indicates position of **(j)**, illustrating the irregular diameter of the filament.

Stable isotope analysis and concentration measurements of nitrogen and carbon were performed simultaneously with a Thermo Finnigan MAT V isotope ratio mass spectrometer, coupled to a Thermo Flash EA 1112 elemental analyzer via a Thermo Finnigan Conflo IV interface in the stable isotope laboratory of the Museum für Naturkunde, Berlin. Isotope ratios are expressed in the conventional delta notation ($\delta^{13}C / \delta^{15}N$) relative to atmospheric N (Mariotti, 1983) and VPDB (Vienna PeeDee Belemnite standard). Standard deviation of repeated measurements of lab standard material (peptone) is generally better than 0.15‰ for both N and C. Standard deviations of concentration measurements of replicates of our lab standard are < 3 % of the concentration analyzed.

FTIR absorption spectra of several small, 40–60 µm wide, translucent dark-brown fragments of kerite (sample no. 0, which showed the least mineralization crust) were measured in the spectral range 7000–700 cm^{-1} at room temperature using a Bruker IFS 66 spectrometer equipped with an IR microscope. The kerite fragments were selected under a binocular microscope and placed on an IR-transparent KBr plate. Spectra were taken in the transmittance mode at a spectral resolution of 4 cm^{-1} with a measuring spot diameter of 40 µm. The reference spectra were measured through the same KBr plate. The time-averaged signal was collected over 200 scans in both reference and sample spectra. For comparison, absorption spectra of chitin (poly-(1,4)-β-N-acetyl-D-glucosamine) and > 75 % deacetylated chitin, or chitosan (2-

amino-2-deoxy-(1,4)-β-D-glucopyranan), both produced by Sigma-Aldrich Chemie GmbH (C7170-100G, C3646-10G) from shrimp shells, were measured in several single flattened, 30–50 µm thick transparent flakes of these materials under the same conditions. Band assignments are based on literature comparison (Table S1).

4 Results

4.1 Morphology

4.1.1 Filaments

Filaments are curvilinear with smooth surfaces and circular cross section (Fig. 3) with different types of ends (Fig. 4). Other types have a structured surface, some are conical, others strongly curved (Figs. 5, 6). Branching is typical for filaments with a smooth surface and was observed as Y, T, and double-T branching (Fig. 3b, h), as multiple branching (Fig. 3c), and combined Y–T branching (Fig. 3d). Clear indications of anastomosing filaments were not found. Multiple branching represents the beginning of growth of filaments (Fig. 3e). In others, globular outgrowths possibly mark the beginning of new branches (Fig. 3g). Whereas the diameter of the individual filaments can be homogeneous between approximately 10 and 20 µm (sample no. 0), others (e.g., sample no. 3; Fig. 3f) show different diameters, between a few micrometers and several tens of micrometers. Ball-shaped outgrowths at the end of a filament occur together with a conical thinning-out filament (sample no. 1; Fig. 3i). Conical, thinning-out filaments originate in Y branching from a thicker filament with constant diameter (Fig. 3m). One object was identified with multiple conical filaments, with claw-like curved ends (sample no. 6; Fig. 3j, k, l). The bottom part can be interpreted as the beginning of growth of the filaments on a substrate, i.e., the clay mineral assemblage in the miarolitic cavities.

Most filaments are broken pieces of larger filaments, and preserved length is on the order of millimeters, and it can be assumed that the original length was up to centimeters. Complete filaments were observed, with one end ball-shaped, the other end thinning out (Fig. 6i, o). Whereas the beginning of a filament is rarely observed, ends are frequently preserved (Fig. 4) and can be either simply round (Fig. 4a), ball-shaped (Fig. 4b–f), rarely with oval shape (Fig. 4e), or conical thinning-out (Fig. 4g, l, m).

Ball-shaped outgrowths (Fig. 4h) and multiple ball-shaped ends (Fig. 4i) possibly mark the beginning of new branches, and balls can be situated asymmetrically at the end of a filament (Fig. 4j). The structured surface of this ball-shaped end is caused by the fossilization process, as indicated by the round pores in the surface, together with mineral incrustation (Fig. 4k). This is also seen on the surface of a 300 µm long conical filament fragment (Fig. 4m, n), which has a micrometer-wide rim of mineral incrustation with a homogeneous interior part (Fig. 4o).

The structured surface is only partly a result of the fossilization process. Figure 5a–f show a filament with approximately 4 mm preserved length and oval cross section (120 × 80 µm thick on one end), which has a dented surface and bulbous outgrowths (Fig. 4d). Another example of a strongly curved filament (Fig. 4g–l) with bulbous surface, several millimeters in length and close to 200 µm diameter, shows irregular segmentation in distances between 35 and 70 µm. On the surface of the filament, relics of a sheath are visible; partly the sheath is intact. The transition between the intact sheath and the remnants exhibits a polygonal structure and circular 1–2 µm wide holes, probably caused by decay/-fossilization. Segmentation is also seen in a branched filament with approximately 3–5 µm wide ridges (Fig. 4m, n, o). This filament has a mineralized outer part of clay minerals with irregular ridges; however, where branching starts, the surface is intact. We interpret these irregular ridges as irregular segmentation of the filament, accentuated and emphasized by fossilization.

Some samples have joint occurrence of filaments with smooth, slightly, and strongly bulbous surfaces (Fig. 6a, b) and joint occurrence of straight, slightly, and strongly curved filaments with irregular segmentation (Fig. 6c, d). The strongly bulbous filaments are transitional to outgrowths (Fig. 6d). Segmentation is indicated (Fig. 6e) and the surface can be strongly sculptured. The filaments have variable diameters from 75 µm (Fig. 6e) to approximately 250 µm (Fig. 6d, f). Some thin filaments show clear indication of segmentation (Fig. 6g, h). The strongly sculptured surface consists of small ball-shaped outgrowths. Joint occurrence of filaments with strongly sculptured surface and smooth surface and with slight striation perpendicular to filament length and filaments with strong sculptured surface (Fig. 6k, l, m, n) indicates that these are probably different types of organisms, not different stages of fossilization.

4.1.2 Hollow objects

Some objects appear hollow (Fig. 7); one object (Fig. 7a, b) has a hollow lower part transitional into a more solid upper, strongly bulbous part. The hollow rather irregular objects (Fig. 7c) occur together with filaments. Filaments can also be hollow (Fig. 7d–h), and the thickness of the outer rim is approximately 2 µm (Fig. 7h). This is the width of the fossilized outer part of filaments, which we documented in the previous study (Franz et al., 2022a), and therefore we interpret the hollow objects as organisms in which the interior part was completely decayed during and after the fossilization process. Some of the hollow objects are bowl-shaped (Fig. 7i–n). One such object (Fig. 8) is > 1 mm large, and from the view in different perspectives is can be seen that it is grown onto mineral substrate; in addition to the clay minerals fluorite is a characteristic mineral and indicates a high fluo-
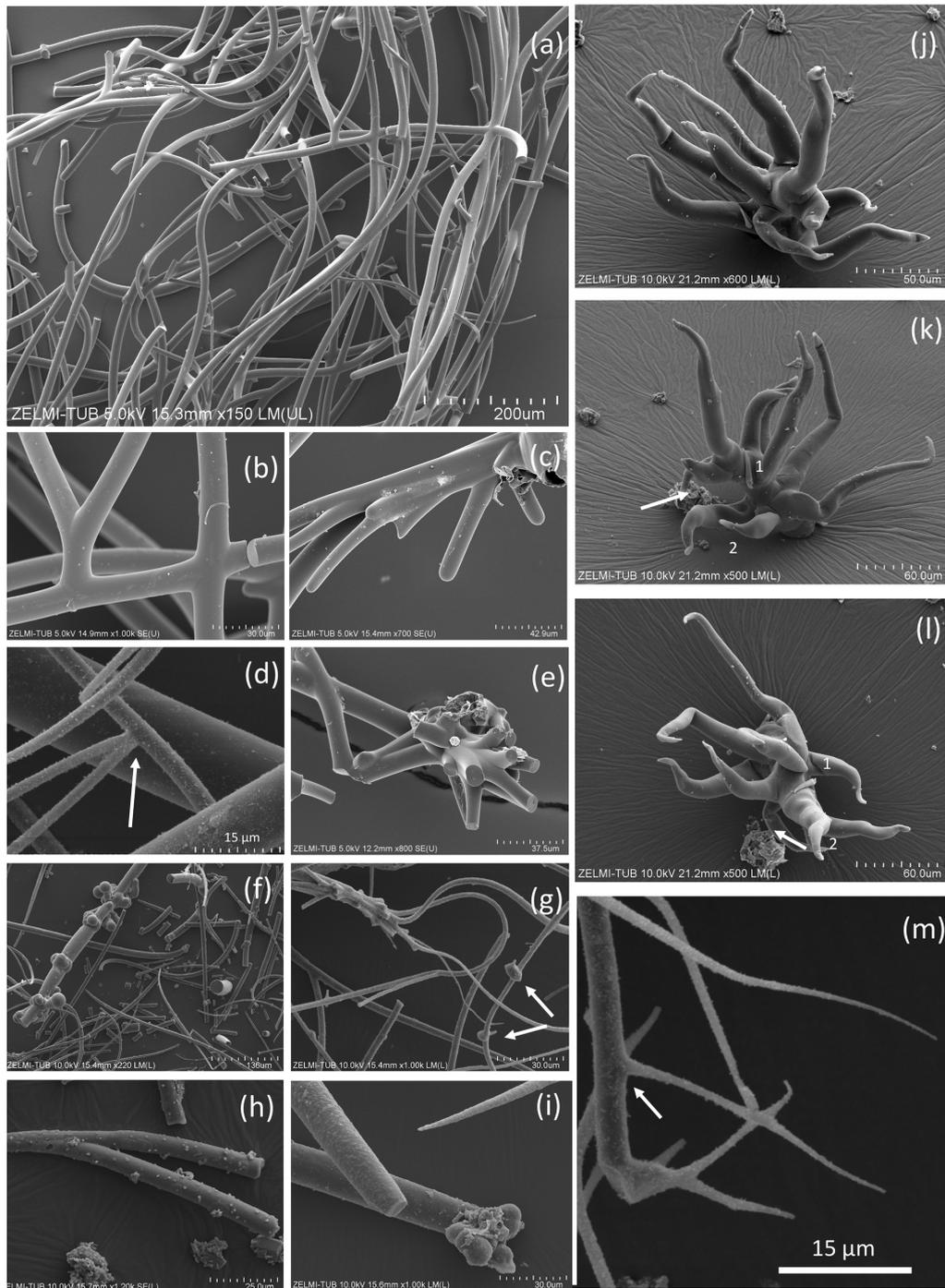
Figure 3. SEM images of curvilinear filaments with smooth surfaces and circular cross section. **(a)** Overview of sample no. 0, illustrating the amount of material with homogeneous diameter of approximately 10 μm, length of more than 1 cm, round ends. **(b)** Branching with Y, T, and double-T junctions. **(c)** Multiple branching and **(d)** combined Y and T branching. **(e)** Possible multiple branching representing the beginning of the filaments. **(f)** Overview (sample no. 3) with filaments of variable diameter and **(g)** multiple branching (upper left) and small outgrowths (arrows). **(h)** Sample no. 4 with Y branching. **(i)** Sample no. 1 showing 3 filaments, one thinning out (upper left), one with constant diameter with ball-shaped outgrowths on end (below), and a slightly conical one (above). **(j, k, l)** Image of multiple, conical filaments with claw-like ends, growing from a common center; view of the same object (sample no. 6) in different perspectives. In **(k)** and **(l)** numbers 1 and 2 identify the same beginning and end of a filament; arrows point to a fluorite crystal. **(m)** Y branching of a thinning-out filament (arrow) starting from a filament with constant thickness. The star-like shape in the center is not branching; it shows different filaments in different heights.
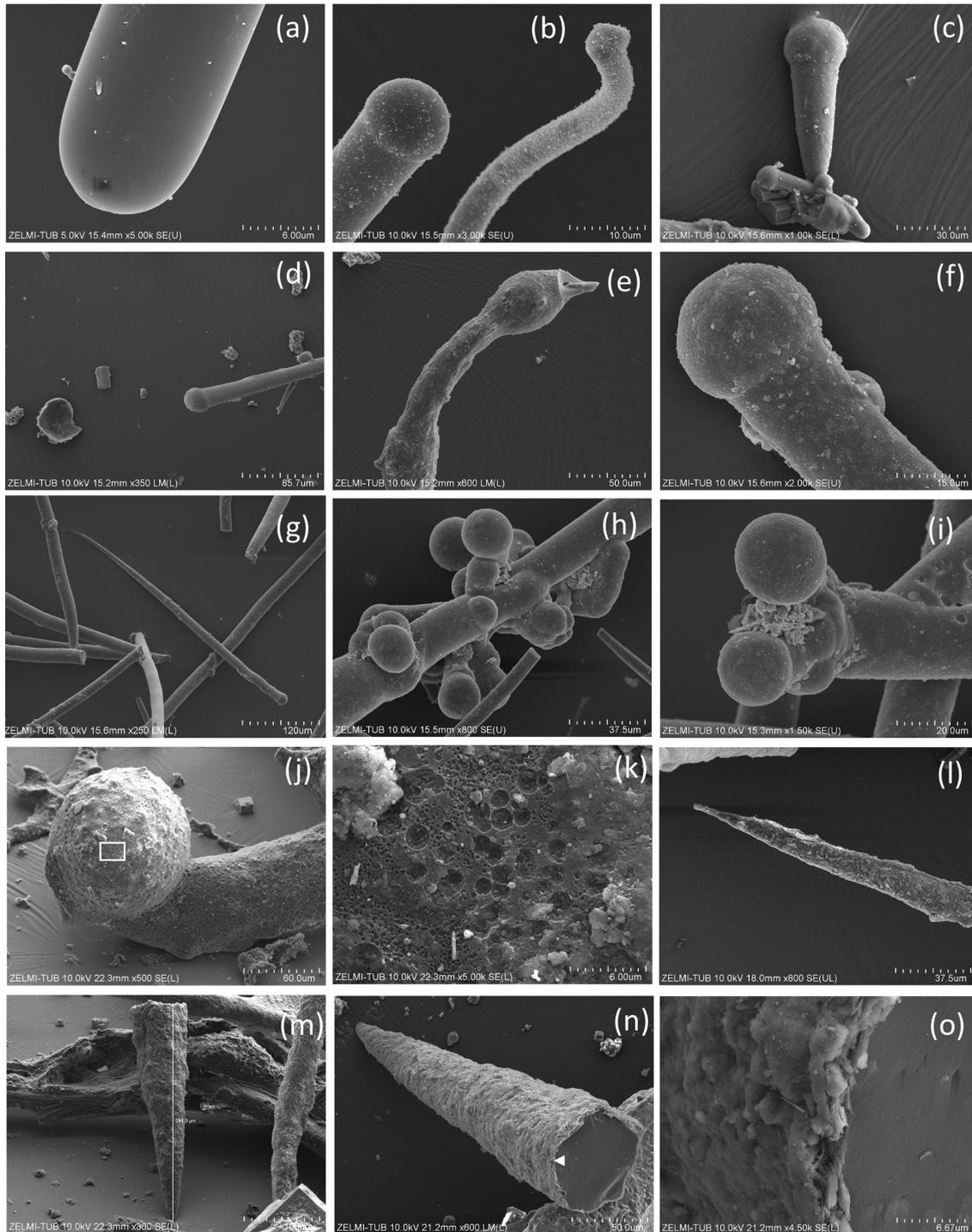
Figure 4. SEM images of ends of filaments with a smooth surface. **(a)** Simple round end (sample no. 0). **(b)** Ball-shaped end of straight and curved filament (sample no. 3). **(c)** Ball-shaped end of conical filament (sample no. 1). **(d)** Ball-shaped end of straight filament (sample no. 5). **(e)** Oval-shaped outgrowths near end of filament (sample no. 7). **(f)** Ball-shaped end (sample no. 1). **(g)** Complete filament with one end thinning out, one with a round end (sample no. 1). **(h)** Ball-shaped outgrowths and ends (sample no. 3). **(i)** Double ball at end of filament (sample no. 1) **(j)** Ball-shaped end; rectangle indicates position of **(k)**, surface of the ball with mineral incrustation and porosity, interpreted as result of decay/fossilization (sample no. 6). **(l)** Thinning-out of a filament (sample no. 5). **(m, n)** Cone-shaped filament in different perspective, approximately 300 μm preserved length (sample no. 6); white triangle indicates position of **(o)** detail of the 1–2 μm wide rim with mineral incrustation.
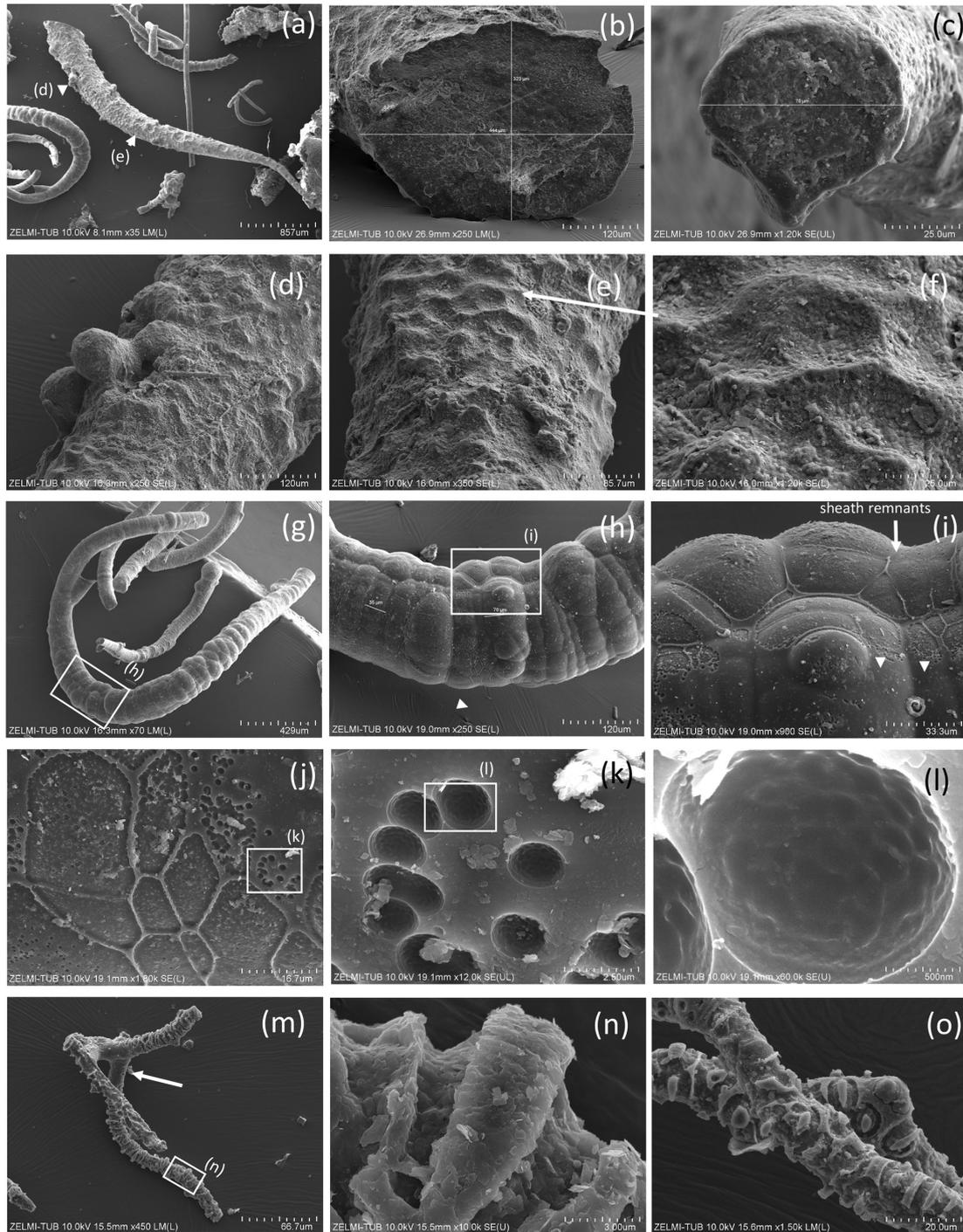
Figure 5. Filaments with structured, rough surface. **(a)** Conical filament of approximately 4 mm preserved length, upper oval diameter **(b)** 440 µm × 320 µm, **(c)** thin end 70 µm (sample no. 5); triangles point to details shown in **(d)**, bulbous outgrowths, and **(e, f)** dented surface. **(g)** Strongly curved filament with bulbous surface, several millimeters in length and close to 200 µm diameter (sample no. 5). Rectangle shows position of **(h)**, bulbous surface with irregular segmentation in distances between 35 and 70 µm; rectangle indicates position of **(i)**, white triangle position of **(j)**. **(i)** In the upper part of the filament, relicts of a sheath are visible (single arrow), in the lower part the sheath is intact (triangles point to the contact). **(j)** The transition between the intact sheath and the remnants in the lower part of the filament exhibits a polygonal structure and **(k, l)** circular 1–2 µm wide holes, probably caused by decay/fossilization. **(m)** Branched filament with approximately 3–5 µm wide ridges (sample no. 2). Note the intact surface where branching starts (arrow). **(n)** Detail of central part of **(m)**. Platy objects are clay minerals. **(o)** Similar feature of filament surface (sample no. 4) with irregular ridges, indicating irregular segmentation.
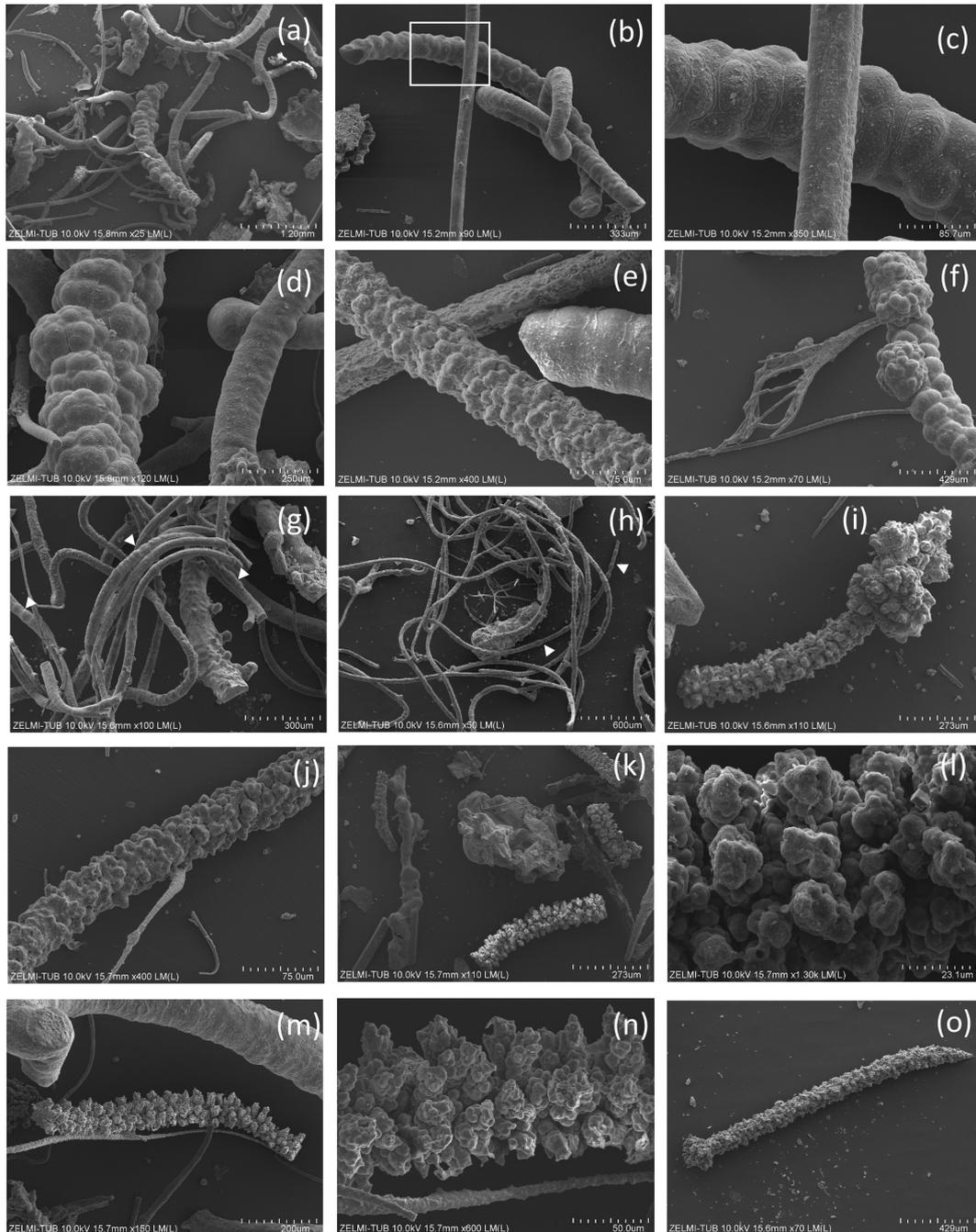
Figure 6. SEM images of filaments with structured, rough surface 2. **(a)** Overview illustrating joint occurrence of smooth, slightly, and strongly bulbous surfaces (sample no. 5). **(b)** Joint occurrence of straight, slightly and strongly curved filaments; rectangle indicates detail in **(c)** with irregular segmentation of the slightly curved filament. The straight filament also shows a slight structure on the surface (lower right). **(d)** Joint occurrence of slightly bulbous (right) and strongly bulbous filaments, transitional to outgrowths. **(e)** Filament with indication of segmentation (right) and filament with strongly sculptured surface; note the small diameter (75 μm) compared to the large filament in **(d)**. **(f)** Thick filament with bulbous outgrowths, next to thin agglutinated filaments. **(g, h)** Thin filaments with indication of segmentation (white triangles). **(i)** Complete filament of approximately 1 mm length with strongly sculptured surface and outgrowths. **(j)** Part of a filament with strongly sculptured surface. **(k)** Joint occurrence of filaments with strongly sculptured surface and smooth surface, together with an irregularly shaped object (center). **(l)** Detail of strongly sculptured surface, which consists of small ball-shaped outgrowths. Note the fluorite crystal in upper right, below label **(m)**, which shows joint occurrence of thick filament (top) with slight striation perpendicular to filament length, and filament with strong sculptured surface, detail shown in **(n)**. **(o)** Almost 2 mm long complete filament: one thin end, one with outgrowths.

rine activity in the fossilizing fluid (Franz et al., 2022a). The base of mineral substrate is followed by an approximately 10 μm thick solid rim with bulbous outgrowths.

4.1.3 Spherical objects

Most spherical objects (Fig. 9) appear as rather complete, with only some parts broken off. One object with a double-ball shape (Fig. 9a, b) is clearly grown onto the substrate (Fig. 9c). The double-ball with remnants of a sheath points to cell separation. Note the different size of the objects from < 10 μm (Fig. 9m) to > 1 mm (Fig. 9g). Two small objects identified on the etched beryl surface appear like seeds or spores (Fig. 9l, m).

4.1.4 Irregular objects

Irregular, flaky objects are abundant, especially on the surface of the beryl crystal (Fig. 2e, f), but also in many samples (e.g., Figs. 6k, 7a, c, o, 8, 9j, k). They show the same fossilization features as the filaments with a thin rim enriched in Si, Al, Ca, and P, loss of N, and oxygenation (Franz et al., 2022a). In some samples (Fig. 6f) filaments appear agglutinated by OM and we interpret these as well as the irregular objects on the beryl crystals as fossilized biofilm.

4.2 Internal structure

For investigation of the internal structure we used SEM images of broken filaments and other objects, as well as polished sections embedded in epoxy, investigated by BSE images including mapping of element distribution. Data of open-pyrolysis and TEM data (Franz et al., 2022a) had shown that the OM is highly mature, amorphous oxy-kerite. Indications of an outer cell wall are absent, because the outer rim of the fossils is silicified, partly with formation of mineral incrustation.

Segmentation of filaments, which might be a characteristic phenomenon for certain organisms and is observed in the filaments' morphology (Figs. 5g, h, 6b, c, e, h), is not obvious in the cross section, but one section shows internal cracks, separating the filament in ~ 50 to 100 μm wide segments (Fig. 10a, b). A section of a bulbous fossil shows cracks, which separate the individual bulbs from each other (Fig. 10g, h).

The outer rim of the filament shows the typical enrichment of Si and Al (Fig. 10b), and the inner, homogenous and not silicified part shows abundant nanometer-sized mineral inclusions (Fig. 10c). They are located in the central part and thus not related to the fossilization process, irregularly distributed or in linear array of several crystals (Fig. 10e, h). The minerals were analyzed with the EDS system, and due to their small size on the order of a few nanometers much smaller than the excitation volume of the electron beam, only mixed analyses with the organic material could be obtained (Table 2). Recalculation of the analyses without the

organic compounds C, O, and N yielded an atomic ratio of Bi : (S,Te) near 1 : 1, indicating minerals such as ingodite Bi(S,Te) or joseite $Bi_4(S,Te)_3$. The example of the bulbous filament (Fig. 10g) with inclusions also shows a Bi(S,Te) mineral, located in the central part. The heterogenous BSE contrast is caused by different trace compounds of Fe and Cu. Element distribution of N and O (Fig. 10j, k) in a bulbous fossil, indicated by different BSE contrast (Fig. 10i), shows an internal structure, possibly indicating a primary separation into different cells, whereas S (Fig. 10l) shows a systematic decrease towards the rims of the object, as a result of decay and/or fossilization.

A very characteristic feature of the filaments is a central channel (Fig. 11), observed in many but not all of the filaments. The cross section of the channel can be six-sided (Fig. 11a–c, m), rectangular (Fig. 11d–f), or round (Fig. 11h–l). The channel diameter is variable and ranges from approximately 0.5 to 25 μm in filaments with an outer diameter between approximately 5 and 100 μm; examples in Fig. 11 show 5 μm with a channel of 260 nm × 550 nm (a), 50 μm with a channel of approximately 20 μm (b), 10 μm with a channel of 2.5 μm × 4 μm (c), 100 μm with a channel of 400 nm × 560 nm (d, e), and 41 μm with a channel of 14 μm (i).

4.3 Stable isotopes and C / N variation

Stable isotopes of C and N were obtained from all bulk samples (Table 1); it was not possible to determine individual fossilized objects. In addition, we determined OM in black opal and OM adherent to topaz (see sample list in Franz et al., 2022a).

Results of $\delta^{13}C$ and $\delta^{15}N$ determination and the molar C / N show a large variation (Fig. 12). All $\delta^{13}C$ values are negative, and for kerite fossils vary between $-47\permil$ (sample 2) and $-31\permil$ (sample 1); $\delta^{15}N$ values vary between ~ 3–$4\permil$ (samples kerite 0, 4) and $\sim 10\permil$ (samples 1, 3). OM associated with opal and topaz (considered "secondary") and buddingtonite, which obtained its N from decayed OM, is less negative and homogeneous in $\delta^{13}C$ with values between $-25\permil$ and $-27\permil$. The C values should be considered maximum values, since alteration either by deep-seated CO_2 from the mafic magmas or from meteoric waters would have increased $\delta^{13}C$. The close group of $\delta^{13}C$ and $\delta^{15}N$ values for secondary OM indicates that during maturation and decay they all have reached a similar value. The variation of the N isotopes is not correlated with the C isotopes, and there is also no correlation with C / N.

4.4 FTIR investigation

All measured FTIR spectra of morphologically different kerite fragments in sample no. 0 are very similar (Fig. 13a) and resemble closely the chitosan spectrum (Fig. 13b); both spectra are dominated by two main groups of absorption
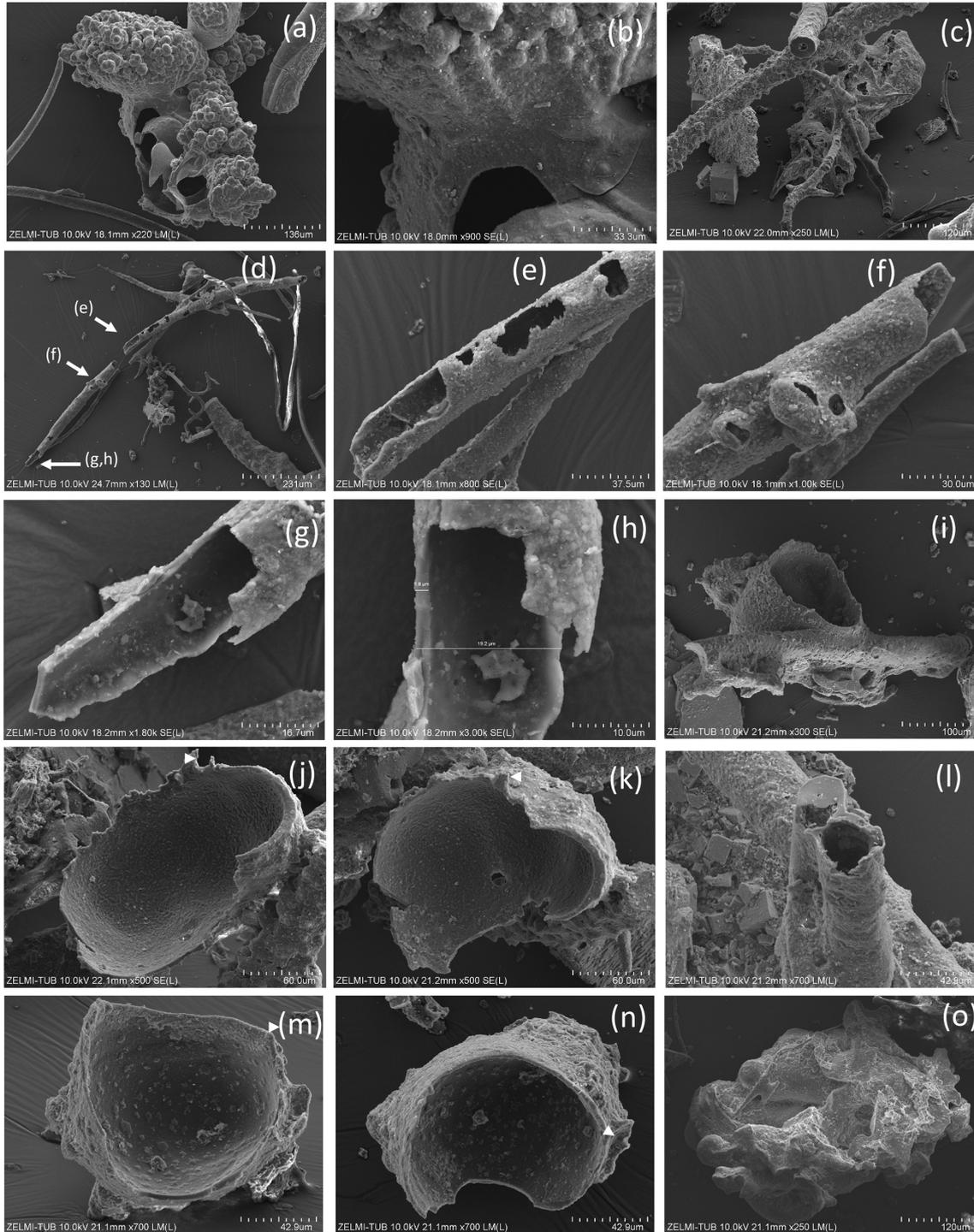
Figure 7. SEM images of hollow objects. **(a)** Irregular-bulbous base of a strongly sculptured object, with **(b)** detail of the transition (center in **a**); sample no. 5. **(c)** Irregular hollow object below filaments (sample no. 6). **(d)** Hollow filament, approximately 1 mm preserved length; position of enlarged parts in **(e)**–**(h)** is indicated (sample no. 5). The mineralized rim is 1–2 μm wide, diameter near 20 μm. **(f)** Bulbous outgrowths are also hollow. **(i)** Filament with an attached hollow form, similar to outgrowths, but much larger (sample no. 6). **(j, k)** Same object as in **(i)**, enlarged in two different perspectives; white triangle indicates identical point. **(l)** Hollow filament next to a filament with a central channel (sample no. 6). **(m, n)** Isolated hollow bowl-shaped object in two different perspectives; white triangle indicates identical point (sample no. 6). **(o)** Irregular object, partly hollow (sample no. 6).
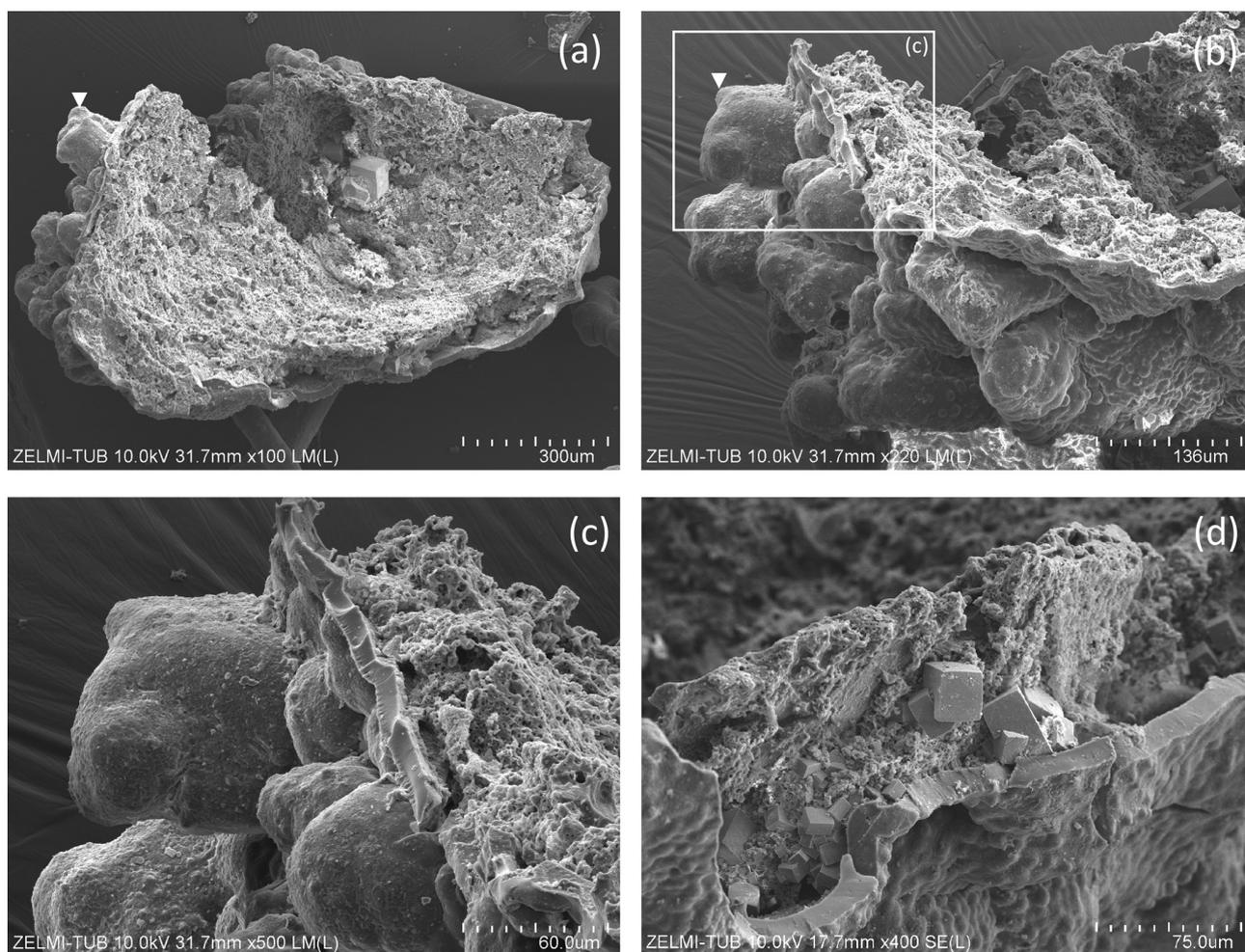
Figure 8. SEM images of > 1 mm large bowl-shaped object (sample no. 5) **(a)** seen from below, grown onto mineral substrate; euhedral crystal is fluorite; white triangle indicates position of **(b)**, enlarged part of the rim. Rectangle indicates position of **(c)** illustrating the base of mineral substrate (right) followed by an approximately 10 μm thick solid rim with bulbous outgrowths. **(d)** Detail of the solid rim with several fluorite crystals.

bands located in the regions of 3500–2500 cm^{-1} and 1800–900 cm^{-1}. The first group consist of overlapping broad bands due to O–H and N–H stretching vibrations, with a group of characteristic narrow peaks of C–H stretching vibrations on their long-wavelength wing in the region of 2960–2870 cm^{-1} (Fig. 13; for detailed band assignments and for spectra of chitin see Table S1). The peak in vicinity of 1650 cm^{-1} is diagnostic of C=O group (Wanjun et al., 2005; Coates, 2011; Loron et al., 2019); the band at 1560 cm^{-1} (broad shoulder near 1570 cm^{-1} in kerite spectra) was assigned to N–H bending vibrations in amide group. The relatively weak band near 1420 cm^{-1} (1450 cm^{-1} in kerite) was attributed to C–H bend (Loron et al., 2019), and the sharp peak at 1380 cm^{-1}, which was reported in cellulose, chitosan, and chitin spectra, was assigned to superposition of the O–H bend (pyranose ring; Li et al., 2009) and symmetrical bend of CH$_3$ group. A band centered near 1315 cm^{-1} in chitin and chitosan spectra due

to C–N stretching vibrations in amide group (Vasilev et al., 2019; Wanjun et al., 2005) is not observed in kerite.

A broad, weak band at around 2100 cm^{-1} is present in spectra of kerite and chitosan (Fig. 13), and the same type of weak bands is shown in published chitosan spectra (see Table S1), but not mentioned and assigned. It can probably be attributed to overtone or combination bands of pyranose ring vibrations. At lower wavenumbers, in all measured spectra there is a series of strong (1150, 1180, 1030 cm^{-1}) and several weak bands caused by different types of C–O vibrations in polysaccharides (Nakamoto, 1997; Wanjun et al., 2005; Li et al., 2009; Coates, 2011; Loron et al., 2019; Vasilev et al., 2019).

A general observation is that in kerite spectra, compared to chitosan, all characteristic absorption bands of the amide group and the pyranose ring become broader and weaker, in agreement with earlier studies of spectroscopic changes
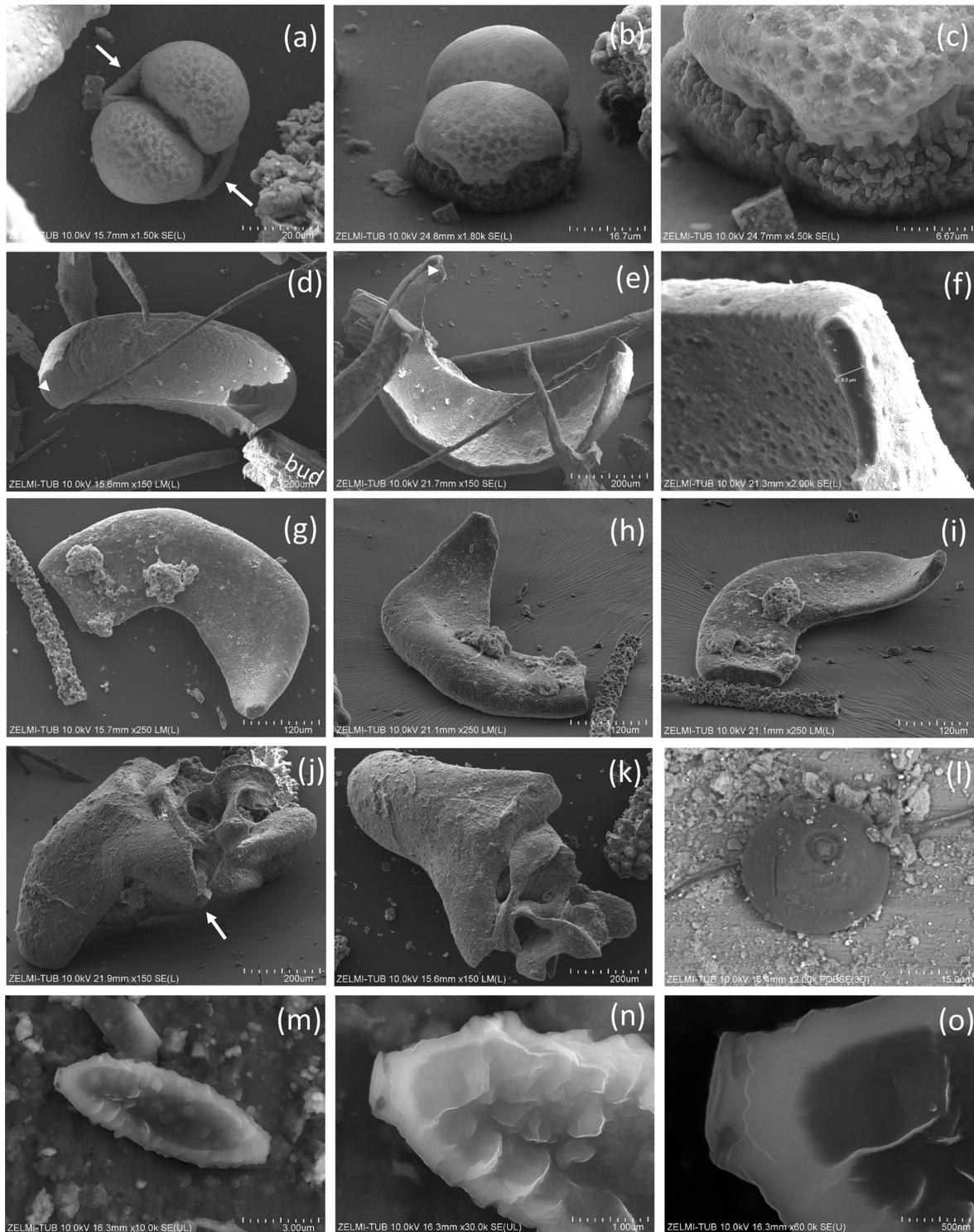
Figure 9. SEM images of spherical objects. **(a, b, c)** Same object in different perspective and magnification; arrows in **(a)** point to a sheath; the euhedral crystal in **(c)** is fluorite. The object grew from a flat mineral surface into a double-ball with dented surface. **(d, e)** Same object in different orientation; white triangle indicates identical position; bud – buddingtonite. **(f)** The thickness measured at one point is approximately 6 μm. **(g, h, i)** Approximately 0.5 mm large object in different perspective with mineral incrustation. **(j, k)** Irregular, partly hollow object in different perspective. **(l)** Perfectly round object, sitting on a filament, on etched surface of beryl (compare Fig. 2d); the circular round structure on its top is beam damage. **(m, n, o)** Oval object on etched surface on beryl (compare Fig. 2i). The lower contrast (dark) in the central part indicates less-dense (partly hollow) material.
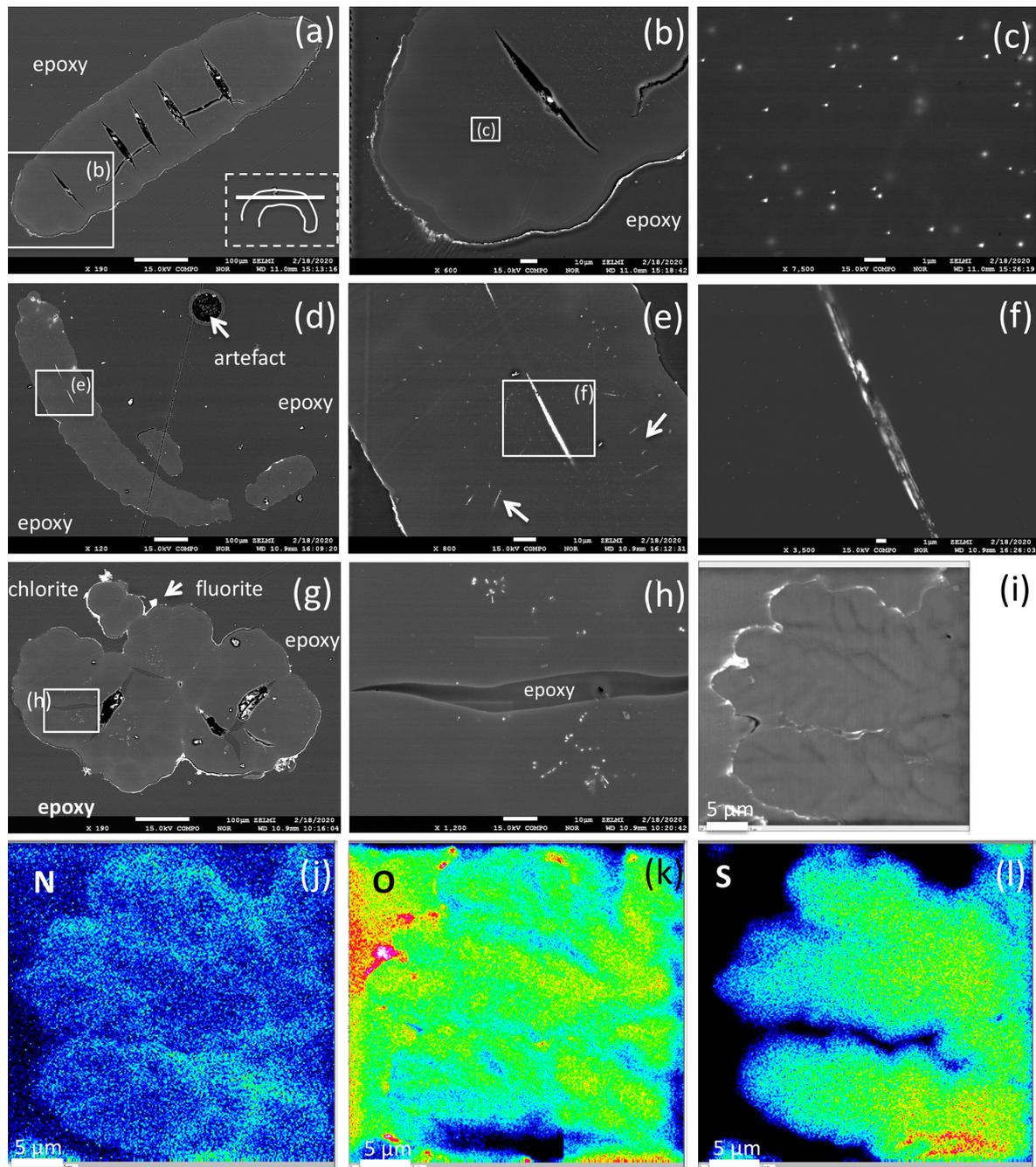
Figure 10. BSE images of filamentous (**a–f**) and bulbous fossils (**g, h, i**), embedded in epoxy, polished thin section, and element distribution (**j, k, l**). (**a**) Part of curved filament; orientation of section is shown in rectangle (dashed lines), position of enlargement (**b**) in rectangle (solid lines). Open cracks (black contrast, with impurities from polishing material) indicate approximately 50 to 100 μm wide segments. (**b**) Silicified outer rim (white contrast, irregular) and a narrow, up to 10 μm wide inner rim are interpreted as the effect of fossilization. The homogeneous appearing central part shows in the enlarged image (**c**) irregularly distributed inclusions, tens of nanometers in size, of Bi–S–Te minerals. (**d**) Filament with two centrally oriented Bi–S–Te mineral inclusions, approximately 50 μm in length and 1–2 μm wide, enlargement shown in (**e**) and (**f**). Arrows in (**e**) point to straight aligned inclusions, and (**f**) shows irregular contrast, possibly caused by heterogeneous distribution of Fe and Cu in the Bi–S–Te minerals. (**g**) Bulbous fossil, with silicified rim and encrustations of chlorite and fluorite. Cracks, partly filled with epoxy, separate individual bulbs from each other. (**h**) Enlarged part showing irregularly distributed and aligned nanometer-sized Bi–S–Te mineral inclusions, and epoxy-filled crack. (**i**) Bulbous fossil with element distribution of N (**j**), O (**k**), and S (**l**), indicating an interior structure with possible former cell walls. The color code goes from cold to warm: blue denotes low concentration, while red denotes high concentration.
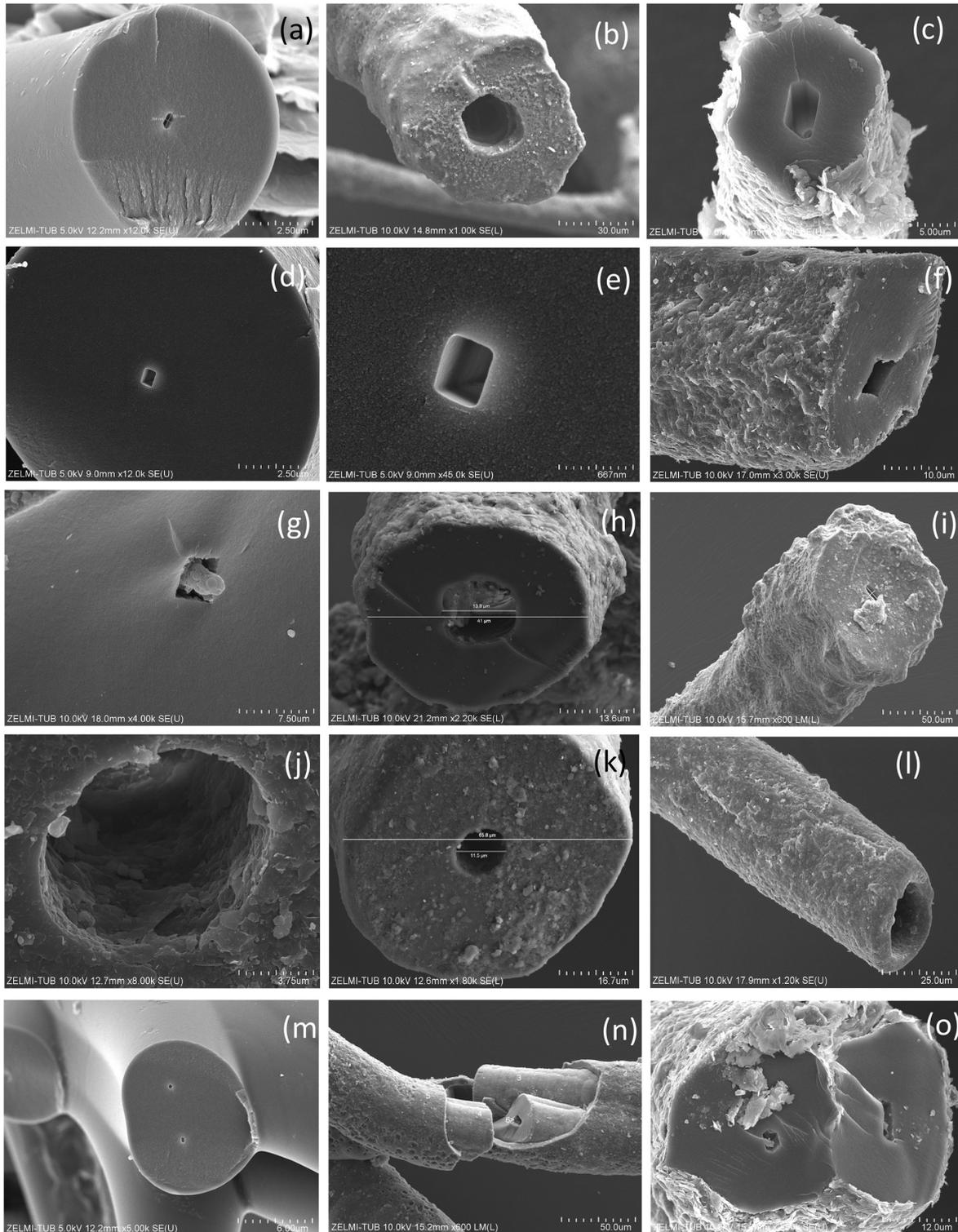
Figure 11. SEM images of broken filamentous fossils, illustrating the central channel. **(a, b, c)** Six-sided channel in filament with **(a)** smooth outer surface, **(b)** dented surface, and **(c)** strongly mineralized surface. **(d, e, f, g)** Rectangular channel; **(e)** is enlarged part of **(d)**. **(h)** Round, slightly irregular channel; **(i)** 4 µm × 6 µm wide channel on filament with dented surface. **(j)** Round channel, enlarged from **(k)**, approximately 12 µm wide in a filament of nearly 70 µm diameter. **(l)** Slightly conical end of a filament with large, round channel. **(m)** Two filaments, with small micrometer-wide channels. **(n)** Channel in a filament with sheath-like structure. **(o)** Two filaments with six-sided channels.

Table 2. EDS analyses of bismuth sulfide telluride inclusions.

Analysis no.	15 06[a]	13 03[b]	13[c] $n = 18$	Min–max
S atom %	0.27	2.59	0.20	n.d.–0.52
Te	0.13	0.06	0.12	n.d.–0.51
Bi	0.29	2.05	0.24	0.01–0.68
Pb	0.03	n.d.	n.d.	
Fe	n.d.	0.19	n.d.	
Cu	n.d.	0.22	n.d.	
C	86.24	84.86	83.38	80.19–96.15
N	5.91	4.89	3.16	n.d.–7.18
O	7.13	5.14	10.12	2.74–15.78
Sum[d]	100	100	100	
Recalculated	15 06	13 03	13 $n = 19$	Min–max
S atom %	38	51	37	3–55
Te	18	1	25	1–90
Bi	40	40	46	7–68
Pb	4	0		
Fe		4		
Cu		4		
Sum	100	100	100	

[a] Fig. 10h. [b] Fig. 10f inclusion in channel. [c] Average of 18 analyses, inclusions in matrix, Fig. 10b, c. [d] Normalized; n.d. – not detected.

Table 3. Results of δ^{15}N, δ^{13}C, and molar C / N of bulk kerite samples.

Sample no.	Weight (mg)	δ^{15}N ‰	mg N per sample	% N	δ^{13}C ‰	mg C per sample	% C	Molar C / N
1	2.76	9.99	0.038	1.37	−30.66	1.91	69.07	58.74
2	2.37	8.44	0.067	2.85	−46.99	0.63	26.52	10.87
3	2.21	10.23	0.027	1.20	−31.38	1.24	56.10	54.58
4	2.52	2.98	0.033	1.31	−33.61	0.44	17.34	15.48
5	4.01	7.37	0.096	2.38	−45.19	0.88	21.98	10.78
6	3.14	7.79	0.037	1.19	−44.06	0.27	8.55	8.39
7	4.29	6.87	0.074	1.73	−43.58	0.71	16.54	11.17
Opal 8	50.15	2.02	0.013	0.03	−25.32	0.55	1.09	49.23
Topaz 9	54.46	1.56	0.023	0.04	−25.73	0.38	0.69	18.89

during chitin/chitosan degradation (Wanjun et al., 2005; Zawadzki and Kaczmarek; 2010; Vasilev et al., 2019). Nevertheless, the main absorption features caused by an amide group, diagnostic of chitosan, are still present in kerite spectra.

5 Discussion

5.1 Interpretation of morphological and internal characteristics

The Volyn biota show an astonishingly large variation of different types of filaments and other forms, pointing to the interpretation that different organisms were involved. We have already interpreted the flaky objects of OM on the surface of

beryl crystals (Fig. 2e, f) as biofilms (Franz et al., 2022a). Agglutinated filaments (Fig. 6f) and the hollow object agglutinated to a filament (Fig. 7i) can similarly be interpreted as fossilized biofilms. The sheath structure (obvious, e.g., in Fig. 5i, j) is also an indication of the presence of a biofilm or extracellular polymeric substance (EPS).

Some objects have a base onto which they grew (Figs. 3j–l, 8, 9a–c), and one object shows a hollow lower part, from which bulbous outgrowths originate (Fig. 7a, b), pointing to sessile organisms. Filaments are generally fragmented, but a few filaments have been found with two intact ends (Figs. 4c, g, 6i, o), and we interpret these as non-sessile, free-living organisms.

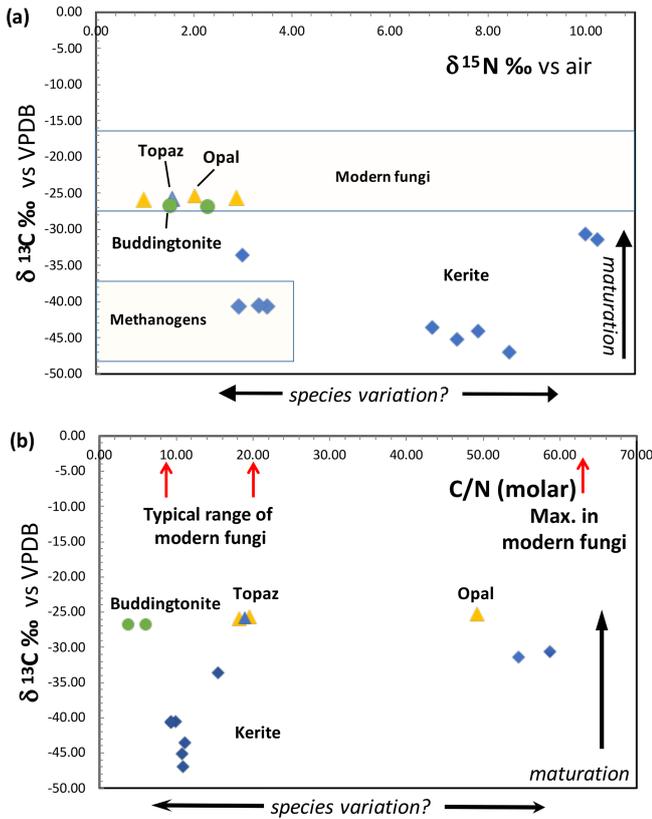Thickness of the filaments varies from ≤ 10 to $> 200\,\mu$m. In filaments with diameters up to approximately $30\,\mu$m,

Figure 12. (a) Results of determination of δ^{13}C and δ^{15}N of Volyn biota and degraded kerite. Symbols: blue diamonds – dominantly filamentous kerite, with small amounts of flaky and spherical OM; yellow triangle – black opal with OM; blue triangle – OM adherent to topaz; green dots – buddingtonite from breccia (from Franz et al., 2017). Fields of modern fungi from Mayor et al. (2009) and methanogens are summarized in Struck (2012). **(b)** Molar C / N ratio of kerite fossils and degraded OM. Range of C / N of modern fungi from Mayor et al. (2009).

Figure 13. FTIR spectra of filamentous fossil compared to standard materials chitin and chitosan. **(a)** Complete spectra of three pieces of sample kerite no. 0, the sample with less mineralization, showing two main regions of absorption: 3500 to 2800 cm^{-1} and 1850 to 900 cm^{-1}. **(b)** Standard material chitosan. Compared to chitosan the major absorption bands in kerite spectra are broader; the weak shoulder near 3100 cm^{-1} in chitosan spectrum is not present in kerite. The narrow triplet near 2950 cm^{-1} is observed as doublet in chitosan, shifted to lower wavenumbers. In the part from 1800 to 700 cm^{-1}, kerite shows only broad absorption, shifted towards higher wavenumbers compared to chitosan, with three superimposed distinct weak peaks at 1450, 1380 and 1038 cm^{-1}; the first is not present in chitosan, which has a number of distinct peaks in this region.

branching with thinning-out of the branch clearly shows that these are within-species variations (irregular diameters of filaments, Fig. 2i, j, are interpreted as collapse structures during fossilization). However, very thick filaments with diameters in the range of $\geq 200\,\mu$m with a structured, bulbous surface (e.g., Fig. 6), or conical objects (Fig. 4m) are interpreted as different species. The length of both types of filaments reaches the millimeter range and, since they are fragments, possibly up to centimeter length.

Branching as an indication of growth of the organisms is typical in the thin filaments, with Y, T, double-T, and multiple branching (Fig. 3), but anastomosing was not observed. In thick filaments with diameters near 200 µm, branching was not found. The ends of filaments also hint to the type of growth. Simple round ends are rare; more typical are ball-shaped ends (Fig. 4). Ball-shaped outgrowths along filaments are interpreted as the beginning of a branching (Fig. 4h). In the complete filaments (Fig. 4c, g) with one end thinning out,
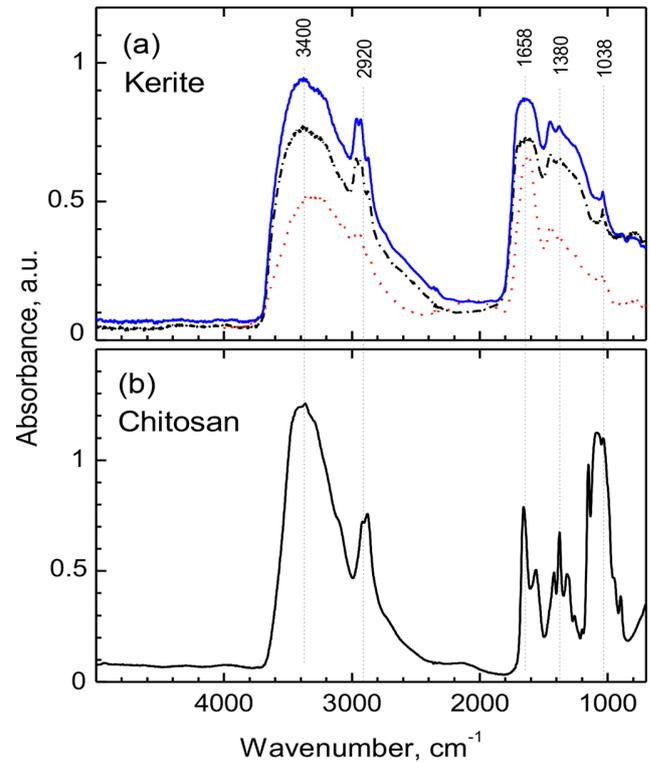
one with a ball-shaped end, the thinning-out end is possibly the origin, the ball-shaped protrusions the growing end, because ball-shaped ends are rather continuous in shape, from a small protrusion (Fig. 4b) to a more complete ball (Fig. 4f, i). Similar protrusions were found at the end of recent, large bacterial filaments (Volland et al., 2022). However, branched, thinning-out ends of the filaments (Fig. 3j–l, m) indicate ends similar to Spitzenkörper, what in modern fungi is described as a continuous and indefinite process of cell extension (Fischer et al., 2008).

Segmentation in thin filaments (Figs. 5m, 6g, h) with distances of a few micrometers up to tens of micrometers is accentuated by mineralization (Fig. 5n), with irregular ridges caused by mineralization. Thick filaments do not show a clear segmentation; the morphology is more irregular and

shows rounded, polygonal structures on the surface with dimensions of approximately 20–30 μm (parallel to filament axis) × 35–70 μm (perpendicular to filament axis) (Figs. 5g, h, i, 6b, c). Between the polygonal structures on the surface, remnants of a sheath are visible. In the cross section (Fig. 10) segmentation is clearly visible by cracks with a distance of approximately 50–100 μm.

Bulbous forms (Figs. 7a, b, 8) mark the beginning of growth of some objects, and bulbous outgrowths are very typical for thick filaments (Fig. 6, d, f), which extend into approximately 20 μm large objects, which consist of smaller bulbs (Fig. 6l, n). In thin filaments with typical branching, the outgrowths are rare and more regularly ball-shaped (Figs. 3f, g, 4h), indicating one species with prominent growth by branching of thin filaments, and another species with growth by outgrowths along thick filaments.

Among the spherical objects, only the small ones with a size of a few micrometers (Fig. 9l–o) resemble spores or other types of seeds/fruit bodies. The irregular, large objects several hundred micrometers in size (Fig. 9d–k) do not fit into any scheme of known organisms. Similarly, there is no obvious interpretation for the large bowl-shaped and irregular hollow objects (Fig. 8). The small double-object with a partly preserved sheath (Fig. 9a–c) grown on a substrate has some similarities with cell division.

The function of the conspicuous central channel (Fig. 11) in many but not all filaments with different shape in cross section is speculative, likely providing pathways for transport of components for cell extension along the filament axis. In one example we observed a type of filling in the channel (Fig. 11g), so in the original organisms it might have been filled with an easily degradable substance. It is not clear whether a hollow form (Fig. 7e, l) is a different phenomenon or due to special preservation conditions. The width of the preserved rim is on the same order of magnitude as the silicified rim (1–2 μm), and therefore it might just be a remnant of a filament, in which the central part was completely degraded.

Another special feature of the internal structure is the nanometer-sized mineral inclusions of Bi–S–Te minerals (Fig. 7). The organisms were able to concentrate these elements, either irregularly distributed (Fig. 7c) or rod-like aligned (in a bulbous object; Fig. 7h) or within the channel (Fig. 7e). It is unclear whether the relatively large Bi–S mineral with some Cu and Fe contents in the center of a thick filament in the central channel is the original position of the Bi–S concentration or an effect of fossilization. Modern fungi are able to concentrate Te (and Se) as nanometer-sized crystals (Liang et al., 2020) and could be used in technology for soil mycoremediation (Liang et al., 2019). In black shales, the organophilic element Bi might behave similarly to Se (Budyak and Brukhanova, 2012). Biogeochemistry of Te is probably analogous to Se (Missen et al., 2020), but little is known about the link of Bi to S and Te in OM (such as in coal; e.g., Finkelman et al., 2019). The concentration

of Bi–S–Te in the organisms of the Volyn biota is another indication of fungi-like organisms, although other organisms such as bacteria are also able to concentrate Te (Missen et al., 2020).

Remnants of cell membranes, separating individual cells, could not be identified, and the answer to the question of whether some of the organisms were multicellular is speculative. However, the large size of many objects of the Volyn biota already indicates that possibly they were not single-celled but multicellular, notwithstanding that single-cell bacteria (*Thiomargarita magnifica*; Volland et al., 2022) can reach the size of centimeters. These macroscopic single-cell bacteria show a very simple straight filament, whereas the large objects from the Volyn biota show a much more complicated form; the surface of large filaments shows a bulbous structure with sizes on the order of tens of micrometers (Figs. 5g–i, 6c, f, 9a, b), well visible with a polygonal network (Fig. 5j). In the internal structure we also see phenomena that could be explained as separate cells, such as the gaps in a filament (Fig. 10a) or in a bulbous object (Fig. 10g). The interior structure visible in the element distribution of N (Fig. 7j) might indicate the original distribution in former interior cell walls, in which chitin-like substance was concentrated. Finally, the small spherical object shown in Fig. 9a and b might be taken as two cells, with an envelope of a sheath.

5.2   Stable isotopes

Modern fungi show a very wide variation of δ^{15}N from -5‰ to $+25$‰, with the main cluster between -5‰ and $+12$‰, and δ^{13}C is restricted to -19‰ to -29‰ δ^{13}C, with the main cluster at -22‰ to -28‰ δ^{13}C (Mayor et al., 2009; Fig. 12a). Whereas the N-isotopic signature of kerite is consistent with the interpretation as fossil fungi, the C-isotopic signature is much lower than that of modern fungi. However, fungi live from consumption of organic matter, and the C-isotopic signature is then transferred to the fungi without a strong isotopic effect (Peterson and Fry, 1987). That is, during incorporation of carbon from modern plants to fungi, the δ^{13}C signature of -27‰ to -30‰ in plants changes to -25‰ to -27.5‰ δ^{13}C in fungi (e.g., Högberg et al., 1999). Assuming that the isotope fractionation in the Volyn biota was similar, the consumed organism had a C-isotopic signature of ca. -35‰ to -50‰ δ^{13}C. These very low values are consistent with the interpretation that the primary organisms were methanogens. Another factor, which must be considered, is intracellular heterogeneity as observed in bacteria (Lepot et al., 2013). The membrane (lipids) can have a signature of 10‰ δ^{13}C lower than the bulk cell, and degradation during fossilization of the proteins and polysaccharides can lower the now determined C signature. It is also possible that the fungi consumed biofilm. Fossil biofilms of the 2.75 Ga Hardey Formation (Australia), probably coexisting with methanogens, methanotrophs, and sulfur-metabolizing

bacteria, have $\delta^{13}C$ of $-55‰$ to $-43‰$ (Rasmussen et al., 2009), well in the range of $\delta^{13}C$ values observed here. The biofilms, described by Rasmussen et al. (2009), lived in synsedimentary cavities similar to stromatolites, pointing to the importance of cavities for the preservation of organic matter, similarly to the biofilms at Volyn in the deep biosphere.

Maturation clearly affects the C- and N-isotope ratios, which we see in degraded OM preserved in black opal, in OM adherent to topaz, and buddingtonite which obtained its NH_4 from OM. These samples have much more positive $\delta^{13}C$ values around $-26‰$ and more homogeneous $\delta^{15}N$ values near $+1.5‰$ to $+3‰$ (Fig. 12a). In contrast, the large variation of $\delta^{15}N$ between $3‰$ and $10‰$ in the kerite samples (Fig. 12a) and C / N between 10 and > 50 (Fig. 12b) possibly indicates a variation of the species. These values were less influenced by maturation, as there is no correlation between $\delta^{13}C$ and C / N in all samples (fossils and degraded OM). Alleon et al. (2018) in their description of the 3.4 Gyr old Strelley Pool microfossils (Western Australia) argued that though the fossils experienced heating up to $300\,°C$, the C / N did not change significantly. Also, for anthracite coal it has been shown that the original C / N did not vary with coalification (Gosh et al., 2020).

Loron et al. (2019) reported fossil fungi from the 1 Ga Grassy Bay Formation, Canada, and provided proof via chitin remnants (FTIR) and showing the characteristic bilayered fungal cell walls (TEM data). However, the few SEM images for the Grassy Bay biota do not allow a comparison with the Volyn biota. Following their discussion, the FTIR investigation of the filamentous Volyn sample shows good indications for preserved chitosan as part of the OM. Degradation studies of chitosan (Wanjun et al., 2005; Zawadzki and Kaczmarek; 2010; Vasilev et al., 2019) showed that the spectra of kerite have the same characteristic bands as chitosan at approximately $250\,°C$; at lower as well as at higher temperatures these bands disappear. Completely independent temperature estimates for the fossilization based on phase equilibria of Be minerals yielded the same temperature range (Franz et al., 2017).

5.3 Taxonomy and comparison with Precambrian biota

Film-like microfossils were described from the 3.4 Gyr old Strelley Pool (Western Australia; Alleon et al., 2018), the 3.3–3.5 Gyr old Onverwacht Group (Australia; Westall et al., 2001), and from the 2.75 Gyr old Hardey Formation (Australia; Rasmussen et al., 2009). There is little doubt that biofilms existed for a long time in the Earth's history and are an integral component of the ancient life cycle (Hall-Stoodley et al., 2004). It seems safe to assume that the irregular (Fig. 2f, and images in Franz et al., 2022a) and sheath-like structures (Figs. 5i,j, 6f, 9a) of the Volyn biota were biofilms.

We have already pointed out that some of the organisms show analogies to fungi. Based on the molecular clock technique, Wang et al. (1999) estimated the divergence between the three-way split of the animal–plant–fungi kingdoms at 1.58 ± 9 Ma, much earlier than the "Precambrian explosion". This age is in the same range as the minimum age of the Volyn biota. Other molecular clock estimates indicate that the first zygomycetous fungi occurred on Earth during the Precambrian, approximately 1.2–1.4 Gyr ago (review in Krings et al., 2013). Diversification of fungi and transition to land was dated at ca. 720 Ma (Lutzoni et al., 2018), and they estimate the origin of fungi at ca. 1240 Ma, similarly to Berbee et al. (2020), who placed the origin of fungi at ca. 1300 Ma. If indeed the Volyn biota contain fungi-like organisms, their origin as well as colonization of land occurred earlier than ca. 1500 Ma.

Bengtson et al. (2017) reported fungus-like organisms in the 2.4 Ga Ongeluk Formation (South Africa) from the deep biosphere, which are however not terrestrial but marine. The important fact is that these fossils were found also in open cavities, though of a completely different size of millimeter amygdales in low-grade metamorphic basalt, in contrast to the huge cavities of tens of meters size in the pegmatites from Volyn. The filaments from the Ongeluk biota with a diameter of ca. 2 to $12\,\mu m$ are generally thinner than the Volyn biota and show anastomosis, but also Y and T branching, and sometimes bulbous protrusions, 5–$10\,\mu m$ in diameter. A special feature is what Bengtson et al. (2017) call "broom structure", diverging filaments growing from a substrate of clay minerals (chlorite), and the filaments consist also of the same type of chlorite. These structures (shown in 2D in thin sections) could be similar to the object from the Volyn biota (Fig. 3j, k, l) and what we called "multiple branching" (Fig. 3c, e, g). A significant difference between the two biota is the fossilization process, which resulted in the Ongeluk biota in complete replacement of the filaments by clay minerals, whereas at Volyn fossilization is restricted to the outermost rim and most of the C is preserved (Franz et al., 2022a).

Good evidence of fungi-like organisms was reported from the early-Ediacaran Doushantuo biota, at approximately 635 Ma (Gan et al., 2021). These fossils are pyritized, but with remnants of organic matter, and consist of branching filaments (Y, T branching, but also with A and H type and anastomosis) and associated hollow spheres. Compared to the Volyn biota, the filaments are thinner (two types, one with average $6.8\,\mu m$, one with average $2.7\,\mu m$), whereas the observable length in thin section with hundreds of micrometers is possibly in the same range as in the Volyn biota. The spheres of the Doushantuo biota are hollow and coaxially aligned but also similar to what we described as ball-shaped outgrowths; their size varies from an average of 16 to $20\,\mu m$ in small ones and large spheres with 36 to $102\,\mu m$, similarly to the Volyn biota (Fig. 4h, i for the small spheres, Fig. 4j for large spheres). The fact that the spheres of the Doushantuo Formation are hollow is possibly due to the fact that they are mostly pyritized; i.e., most of the organic matter was decom-

posed. The small spheres were interpreted (Gan et al., 2021) as possible spores; the larger ones were possibly symbiontic organisms living together with the fungi.

Myxomycetes (slime molds) are other possible eukaryotes, which might have existed in the Proterozoic, although Stephenson et al. (2008) considered 50 Myr as the oldest fossil record. Their diverse morphology during the different stages of their life cycle including amoeboid forms leaves much room for speculation. Filamentous millimeter-long sporocaps, such as shown in Fig. 3a in Rikkinen et al. (2019), are similar to what we see in Fig. 4b. The structured surfaces shown in Fig. 6 are somehow similar to what Dagamac et al. (2017) showed in their Figs. 7–9 from recent *Arcyria complex*, though on the micrometer scale, whereas those from the Volyn biota are much larger. The image of multiple, conical filaments with claw-like ends, growing from a common center (Fig. 3j, k, l), is similar to *Copromyxa protea* shown by Schnittler et al. (2012) in their Fig. 4-2. Hollow objects (Fig. 7, i–k, m, n) resemble open sporocaps of *Licea* sp. (Schnittler et al., 2012, in their Fig. 5-12). Finally, large objects such as the open, bowl-shaped one with bulbous outgrowths (Fig. 8) could be interpreted as the plasmodium of a myxomycete with beginning development of fruiting bodies (e.g., Fig. 2, life cycle of myxomycetes, transition from stage H1 to A; Stephenson and Schnittler, 2016).

Other possible organisms described from the Precambrian are all different from the Volyn biota and are excluded as possible analogs. Palynomorphs, which are among the earliest clear records of terrestrial life (Wellman and Strother, 2015), the 1.67 Gyr old eukaryotic Changcheng biota (Miao et al., 2019), or vase-shaped metazoan microfossils, considered as the oldest evidence for heterotrophic protists (e.g., Urucum Formation, Brazil; Morais et al., 2017), have a very different morphology.

Most of the Precambrian biota listed in the literature are considered photosynthetic organisms, probably not a likely analog for the Volyn biota. For example, the 770 Ma (Cryogenian) Chichkan Formation in Maly Karatau, Kazakhstan (Sergeev and Schopf, 2010), contains biota in fine-grained black chert, which were deposited in a mid-shelf and a near-shore environment with stromatolites. Most of the biota listed by Sergeev and Schopf (2010) are cyanobacteria, rather small mostly up to the 10 μm range and thus do not serve as analogues for the Volyn biota. They also list a number of larger protista (*incertae sedis*) in the 100 μm range, however with little morphological similarity to the Volyn biota. No similarity was found to eukaryotes (acritarchs) from 1.1 Gyr old Taoudeni Basin, Mauretania (Beghin et al., 2017). Red algae (Rhodophyta) from the 1.05 Ga Hunting Formation, considered among the oldest eukaryotes (Butterfield, 2000; Gibson et al., 2018), are photosynthetic organisms and can also be excluded.

5.4 Model for a Precambrian deep biosphere ecosystem

The Volyn occurrence is a well-preserved example of a fossil ecosystem of the deep continental biosphere. We exclude an abiotic origin as previously postulated (Ginzburg et al., 1987; Luk'yanova et al., 1992) because of the extremely low δ^{13}C values and the large variation in morphology. Abiotic pseudofossils have been produced experimentally, e.g., by Nims et al. (2021) and references therein, when sulfide is oxidized in the presence of organics. These "organic biomorphs" show a large variety of morphologies, mostly filamentous, but also globular. In a siliceous environment (for many cases chert) such organic biomorphs can be replaced by silica, and their morphology can be well preserved. However, for the Volyn biota such a sulfide-rich environment did not exist. Additionally, we take the presence of chitosan as another indication of a true fossil. McMahon (2019) provided another example of pseudo-fossils, which is however restricted to an iron-rich environment; these pseudo-fossils consist of hematite or iron oxides–hydroxides, conditions not realized in the highly differentiated pegmatites, which are very poor in Fe. Rouillard et al. (2018) produced another type of pseudofossils with an amazing large variety of morphologies, which might occur in hydrothermal, silica-rich rocks, but require a high activity of Ba, for which there is no indication in the Volyn pegmatites.

In combination with textural arguments, the age determination of muscovite, formed in pseudomorphs after beryl, points to a minimum age of 1.5 Ga (Franz et al., 2022b); the maximum age is restricted by the intrusion of the igneous rocks at 1.760 Ga (Shumlyankyy et al., 2021).

The geological context argues for a continental, terrestrial environment, because the KPC intruded into continental crust most likely in a within-plate tectonic setting (Shumlyanskyy et al., 2012, 2017). After intrusion uplift to the erosion level occurred, documented by an unconformity, sedimentation started with sandstones and shales at approximately 1.4 Ga (Zbranki Formation; Gorokov et al., 1981), later than or coeval with the pseudomorph formation and the minimum age of the microfossils. The depth, where the organisms lived, is an open question, but the occurrence in the underground mines indicates a depth of up to at least 150 m. The age of 1.5 Ga is much later than the Great Oxidation Event of the Earth's atmosphere, allowing for the evolution of complex species and ecosystems on the land (sub)surface. The supply of organic matter to the underground for the production of the high amounts of kerite is speculative. In a geyser system, which we invoke for the whole geological situation, intense growth of organisms at the surface is a common observation. In such systems continuous exchange between surface and depth is evident. This also excludes the very deep (more than several hundreds of meters) biosphere. The biota were more likely located near to the surface. Unfortunately, no information is available right now on which of the many pegmatites from the Volyn pegmatite field con-

tain kerite and which – in what depth – are devoid of kerite. This remains to be investigated in the future.

Drake et al. (2017) reported partly mineralized fungi from the deep continental (granitic) biosphere (up to 740 m). The fossilization process also included maturation of the OM and final mineralization by clay minerals. The source of carbohydrates was living or dead bacterial biofilms, similar to what we speculate about the Volyn biota.

The large size of the filaments up to a centimeter in length is atypical for bacteria and archaea. Although Volland et al. (2022) described recent centimeter-long bacteria, these are still the exception, and it is more likely that some of the Volyn biota were multi-cellular eukaryotes. Their suggested age of 1.5 Ga is the age range given for the first appearance of eukaryotes (see review in Butterfield, 2015). Putative centimeter-sized Precambrian fossils (different from the Volyn biota) were reported from the 2.1 Gyr old Francevillian biota (El Albani et al., 2014); however, they are completely pyritized and occur in diagenetically overprinted black shales, which makes the interpretation difficult.

The Volyn biota must have been highly radiation resistant, because a U–Th–K-rich granitic–pegmatitic system has a high radiation level. There are a number of different organisms, such as bacteria (e.g., *Deinococcus radiodurans*), archaea (*Thermococcus gammatolerans*) or microscopic fungi (e.g., *Cladosporium sphaerospermum*), which fulfill this requirement; see review in Matusyak (2016). During the mining operations in Soviet times, a high Rn content was measured inside cavities, when they were broken into. The general radiation levels, 3000 times higher than the allowed limit at that time, were even higher 1.5 billion years ago. Deeply black-colored quartz crystals in the pegmatites are of the "morion" type and also indicate high radiation. Recent observations at the Chernobyl power plant have led to speculation about radiotrophic fungi (e.g., Matusiak, 2019; Prothmann and Zauner, 2014), which produce melanin as a protection against radiation and enhancement of fungal growth via capture of ionizing radiation for energy conversion (Dadachova et al., 2007; Tugay et al., 2017). Mycoremediation is at least a well-documented mechanism for a very effective method of radio nuclide pollutant removal considering the versatility of fungi in terms of their ecology, nutritional modes, adaptability, morphology, physiology, and metabolism (Shourie and Vijayalakshmi, 2022). Fungi are known as extremophilic organisms (e.g., Blachowicz et al., 2019), and we can expect that in the Proterozoic or possibly already earlier in the Earth's history similar organisms were active and resistant to a high radiation level, in an epoch when the ozone layer was not yet fully developed.

6 Summary and conclusions

The exceptional 3D preservation of the 1.5 Ga Volyn biota is due to the fossilization conditions in open cavities, with SiF$_4$-rich fluids as the driving agent. There are a number of indications that fungi-like organisms were likely an important part of the microecosystem – filaments with branching (though not anastomosing), growth in thinning-out ends, and also in bulbous extrusion, both at the end of filaments and along the filaments. Sheath-like structures are clearly visible, and there are good indications of a former biofilm and extracellular proteinic substance. The large size and internal structure of the organisms and the segmentation visible on thick filaments points to multicellular organisms, and the nano-sized inclusions of Bi(S,Te) crystals have an astonishingly good analog in recent fungi. Other organisms, which might have been present in this subsurface microecosystem, are myxomycetes or myxomycete-like. The stable N- and C-isotopic signature is in accordance with such an interpretation.

The fungi-like organisms possibly lived from lithotrophic methanogens; alternatively or additionally bacteria such as cyanobacteria were transported from the surface downwards into the cavities. The geyser system of the Korosten Pluton provided an ideal framework for growth of bacterial or algal organisms at the surface. In the deep biosphere, attached as well as free-living forms of organisms are observed.

The Volyn biota show that fungi-like organisms developed before 1 Ga (Loron et al., 2019), and support the speculation that the fossils from the 2.4 Ga Ongeluk Formation were fungi-like organisms (Bengtson et al., 2017). Molecular clock data, especially the three-way split of the kingdoms animals–plants–fungi at 1.58 ± 9 Ma (Wang et al., 1999), are still uncertain, but our data indicate that it must have occurred early in the Proterozoic.

The Volyn biota also prove that a deep continental biosphere was already present in the early Mesoproterozoic/late Paleoproterozoic. It is known that in the subseafloor environment microbial life existed in the Archean (Cavalazzi et al., 2021), as described from the 3.4 Gyr old Onverwacht Group of the Barberton greenstone belt, but from the continental environment this has not yet been reported.

References

Alleon, J., Bernard, S., Le Guillou, C., Beyssac, O., Sugitani, K., and Robert, F.: Chemical nature of the 3.4 Ga Strelley Pool microfossils, Geochem. Persp. Lett., 7, 37–42, https://doi.org/10.7185/geochemlet.1817, 2018.

Beghin, J., Storme, J.-Y., Blanpied, C., Gueneli, N., Brocks, J. J., Poulton, S. W., and Javaux, E. J.: Microfossils from the late Mesoproterozoic – early Neoproterozoic Atar/El Mreiti Group, Taudeni basin, Mauretania, northwestern Africa, Prec. Res., 291, 63–82, 2017.

Bengtson, S., Rasmussen, B., Ivarsson, M., Muhling, J., Broman, C., Marone, F., Stampanomi, M., and Bekker, A.: Fungus-like mycelial fossils in 2.4 billion-year-old vesicular basalt, Nat. Ecol. Evol., 1, 1–6, 2017.

Berbee, M. L., Strullu-Derrien, C., Delaux, P.-M., Strother, P. K., Kenrick, P., Selosse, M.-A., and Taylor, J. W.: Genomic and fossil windows into the secret lives of the most ancient fungi, Nat. Rev. Microbiol., 18, 717–730, 2020.

Blachowicz, A, Chiang, A. J., Elsaesser, A., Kalkum, M., Ehrenfreund, P., Totok, T., Wang, C. C. C., and Venkateswaran, K.: Protemoic and mteabolic characteristics of extremophilic fungi under simulated Mars conditions, Front. Microbiol., 10, 1013, https://doi.org/10.3389/fmicb.2019.01013, 2019.

Budyak, A. E. and Brukhanova, N. N.: Selenium, bismuth, and mercury in black shale-hosted gold deposits of different genetic types, Geochem. Int., 50, 791–797, 2012.

Butterfield, N. J.: Bangiomorpha pubescens n. Gen., n. sp.: Implications for the evolution of sex, multicellularity, and the Mesoproterozoic/Neoproterozoic radiation of the eukaryotes, Paleobiology, 26, 386–404, 2000.

Butterfield, N. J.: Early evolution of the eukarya, Palaeontology, 58, 5–17, https://doi.org/10.1111/pala.12139, 2015.

Cavalazzi, B., Lemelle, L., Siminovici, A., Cady, S. L., Russell, M. J., Bailo, E., Canteri, R., Enrico, E., Manceau, A., Maris, A., Salomé, M., Thomassot, E., Bouden, N., Tucoulou, R., and Hofman, A.: Cellular remains in a $\sim$ 3.42-billion-year-old subseafloor hydrothermal environment, Sci. Adv., 7, eabf3963, https://doi.org/10.1126/sciadv.abf3963, 2021.

Coates J.: Interpretation of infrared spectra, a practical approach, Encyclopedia of Analytical Chemistry, edited by: Meyers, R. A., John Wiley & Sons Ltd., ISBN: 0471976709, 9780470973332, 2011.

Dadachova, E., Bryan, R. A., Huang, X., Moadel, T., Schweitzer, A. D., Aisen, P., Nosanchuck, J. D., and Casedevall, A.: Ionization radiation changes the electronic properties of melanin and enhances the growth of melanized fungi, PLoS ONE, 5, 1–13, 2007.

Dagamac, N. H., Dela Cruz, T. E., Rea-Maninta, M. A. D., Aril-Dela Cruz, J. V., and Schnittler, M.: Rapid assessment of myxomycete diversity in the Bicol Peninsula, Phillipines, Nova Hedwigia, 104, 31–46, 2017.

Drake, H., Ivarsson, M., Bengtson, S., Heim, C, Siljeström, S., Whitehouse, M. M., Broman, C, Belivanova, V., and Åström, M. E.: Anaerobic consortia of fungi and sulfate reducing bacteria in deep granite fractures, Nat. Commun., 8, 55, https://doi.org/10.1038/s41467-017-00094-6, 2017.

El Albani, A., Bengtson, S., Canfield, D. E., Riboulleau, Bard, C. R., Macchiarelli, R., Ngombi Pemba, L., Hammarlund, E., Meunier, A., and Moubiya Mouele, I.: The 2.1 Ga old Francevillian biota: Biogenecity, taphonomy and biodiversity, PLoS ONE, 9, e99438, https://doi.org/10.1371/journal.pone.0099438, 2014.

Finkelman, R. B., Dai, S., and French, D.: The importance of minerals in coal as the hosts of chemical elements: A review, Int. J. Coal Geol., 212, 103251, https://doi.org/10.1016/j.coal.2019.103251, 2019.

Fischer, R., Zekert, N., and Takeshita, N.: Polarized growth in fungi – interplay between the cycloskeleton, positional markers and membrane domains, Molec. Microbiol., 68, 813–826, 2008.

Franz, G., Khomenko, V., Vishnyevskyy, A., Wirth, R., Nissen, J., and Rocholl, A.: Biologically mediated crystallization of buddingtonite in the Paleoproterozoic: Organic-igneous interactions from the Volyn pegmatite, Ukraine, Am. Mineral., 102, 2119–2135, 2017.

Franz, G., Lyckberg, P., Khomenko, V., Chournousenko, V., Schulz, H.-M., Mahlstedt, N., Wirth, R., Glodny, J., Gernert, U., and Nissen, J.: Fossilization of Precambrian microfossils in the Volyn pegmatite, Ukraine, Biogeosciences, 19, 1795–1811, https://doi.org/10.5194/bg-19-1795-2022, 2022a.

Franz, G., Sudo, M., and Khomenko, V.: ^{40}Ar / ^{39}Ar dating of a hydrothermal pegmatitic buddingtonite–muscovite assemblage from Volyn, Ukraine, Eur. J. Mineral., 34, 7–18, https://doi.org/10.5194/ejm-34-7-2022, 2022b.

Gan, T., Luo, T., Pang, K., Zhou, Ch., Zhou, G., Wan, B., Li, G., Yi, Q., Czaja, A. D., and Xiao, S.: Cryptic terrestrial fungus-like fossils of the early Ediacaran Period, Nat. Commun., 12, 641, https://doi.org/10.1038/s41467-021-20975-1, 2021.

Gibson, T. M., Shih, P. M., Cumming, V. M., Fischer, W. W., Crockford, P. W., Hdgekiss, M. S. W., Wörndle, S., Creaser, R. A., Rainbird, R. H., Skulski, T. M., and Halverson, G. P.: Precise age of Bangiomorpha pubescens dates the origin of eurkaryotic photosynthesis, Geology, 46, 135–138, 2018.

Ginzburg, A. I., Bulgakov, V. S., Vasilishin, I. S., Luk'yanova, V. T., Solntseva, L. S., Urmenova, A. M., and Uspenskaya, V. A.: Kerite from pegmatites of Volyn, Dokl. Akad. Nauk SSSR, 292, 188–191, 1987 (in Russian).

Gorlenko, V. M., Zhmur, S. I., Duda, V. I., Osipov, G. A., Suzina, N. E., and Dmitriev, V. V.: Fine structure of fossilized bacteria in Volyn kerite, Orig. Life Evol. Biosph., 30, 567–577, 2000.

Gorokov, I. M., Clauer, N., Varshavskaya, E. S., Kutyavin, E. P., and Drannik, A. S.: Rb-Sr ages of Precambrian sediments from the Ovruch Mountain range, Northwestern Ukraine (U.S.S.R.), Precam. Res., 6, 55–65, 1981.

Gosh, S., Varma A. K., Das, S. K., Pal, D., and Solanki, G.: Metamorphic tranformations of nitrogen functionalities: Stabilization of organic nitrogen in anthracite and its effect on δ^{15}N parameter, Mar. Petrol. Geol., 112, 104090, https://doi.org/10.1016/j.marpetgeo.2019.104090, 2020.

Hall-Stoodley, L., Costerton, J. W., and Stoodley, P.: Bacterial biofilms: From the natural environment to infectious diseases, Nat. Rev. Microbiol., 2, 95–108, 2004.

Högberg, P., Plamboeck, A. H., Taylor, A. F. S., and Fransson, P. M. A.: Natural ^{13}C abundance reveals trophic status of fungi and host-origin of carbon in mycorrhizal fungi in mixed forests, P. Natl. Acad. Sci. USA, 96, 8534–8539, 1999.

Ivanovich, P. V. and Alekseevich, D. S.: Mineralogy of the Volynian chamber pegmatites, EKOST Association, Mineral. Almanac, 12, 128 pp., Moscow, 2007.

Krings, M., Taylor, T. N., and Dotzler, N.: Fossil evidence of the zygomycetous fungi, Persoonia, 30, 1–10, 2013.

Lepot, K., Williford, K. H., Ushikubo, T., Sugitani, K., Mimura, K., Spicuzza, M. J., and Valley, J. W.: Texture-specific isotopic compositions in 3.4 Gyr old organic matter support selective preservation in cell-like structures, Geochim. Cosmochim. Ac., 112, 66–86, 2013.

Li, J., Zhang, L.-P., Peng, F., Bian, J., Yuan, T.-Q., Xu, F., and Sun, R.-C.: Microwave-assisted solvent-free acetylation of cellulose with acetic anhydride in the presence of iodine as a catalyst, Molecules, 14, 3551–3566, https://doi.org/10.3390/molecules14093551, 2009.

Liang, X., Perez, M. A. M.-J., Nwoko, K. C., Egbers, P., Feldmann, J., Csentenyi, L., and Gadd, G. M.: Fungal formation of selenium and tellurium nanopartikels, Appl. Microbiol. Biotechnol., 103, 7241–7259, 2019.

Liang, X., Perez, M. A. M.-J., Zhang, S., Song, W., Armstrong, J. G., Bullock, L. A., Feldmann, J., Parnell, J., Csentyi, L., and Gadd, G. M.: Fungal transformation of selenium and tellurium located in a volcanogenic sulfide deposit, Environ. Microbiol., 22, 2346–2364, 2020.

Loron, C. C., François, C., Rainbird, R. H., Turner, E. C., Borensztajn, S., and Javaux, E. J.: Early fungi from the Proterozoic era in Arctic Canada, Nature, 570, 232–235, 2019.

Luk'yanova, V. T., Lobzova, R. V., and Popov, V. T.: Filaceous kerite in pegmatites of Volyn, Izvestiya Ross. Akad. Nauk Ser. Geologicheskaya, 5, 102–118, 1992 (in Russian).

Lutzoni, F., Nowak, M. D., Alfaro, M. E., Reeb, V., Miadlikowska, J., Krug, M., A. Arnold, E., Lewis, L. A., Swofford, D. L., and Hibbelt, D.: Contemporaneous radiations of fungi and plants linked to symbiosis, Nat. Commun., 9, 1–11, 2018.

Lyckberg, P., Chornousenko, V., and Wilson, W. E.: Famous mineral localities: Volodarsk-Volynski, Zhitomir Oblast, Ukraine, Mineral. Record, 40, 473–506, 2009.

Lyckberg, P., Chournousenko, V., and Chournousenko, O.: Giant heliodor and topaz pockets of the Volodarsk chamber pegmatites, Korosten pluton, Ukraine, 36th Intern. Gemm. Conf., Nantes, France, 78–83, 2019.

McMahon, S.: Earth's earliest and deepest purported fossils may be iron-mineralized chemical gardens, Proc. Roy. Soc. B, 286, 20192410, https://doi.org/10.1098/rspb.2019.2410, 2018.

Mariotti, A.: Atmospheric nitrogen is a reliable standard for natural ^{15}N abundance measurements, Nature, 303, 685–687, 1983.

Mayor, J. R., Schuur, E. A. G., and Henkel, T. W.: Elucidating the nutritional dynamics of fungi using stable isotopes, Ecol. Lett., 12, 171–183, 2009.

Matusyak, D. M.: Radiotolerant microorganisms – characterization of selected species and their potential usage, Adv. Microbiol., 55, 182–194, 2019.

Miao, L. Y., Moczydłowska, M., Zhu, S. X., and Zhu, M. Y.: New record of organic- walled, morphologically distinct microfossils from the late Paleoproterozoic Changcheng Group in the Yanshan Range, North China, Precam. Res., 321, 172–198, 2019.

Missen, O. P., Ram, R., Mills, S. J., Etschmann, B., Reith, F., Shuster, J., Smith, D., J., and Brugger, J.: Love is in the Earth: A review of tellurium (bio)geochemistry in surface environments, Earth Sci. Rev., 204, 103105, https://doi.org/10.1016/j.earthscirev.2020.103150, 2020.

Morais, L., Fairchild, T. R., Lahr, D. J. G., Rudnitzki, I. D., Schopf, J. W., Garcia, A. K., Kudryavtsev, A. B., and Romero, G. R.: Carbonaceous and siliceous Neoproterozoic vase-shaped microfossils (Urucum Formation, Brazil) and the question of early protistan biomineralization, J. Paleontol., 91, 393–406, https://doi.org/10.1017/jpa.2017.16, 2017.

Nakamoto, K.: Infrared spectra of inorganic and coordination compounds, Parts A and B, New York: Wiley, p. 328, John Wiley & Sons, New York, ISBN: 978-0-471-74493-1, 1997.

Nims, C., Lafond, J., Alleon, J., Templeton, A. S., and Cosmidis, J.: Organic biomorphs may be better preserved than microorganisms in the early Earth sediments, Geology, 49, 629–634, https://doi.org/10.1130/G48152.1, 2021.

Petersen, B. M. and Fry, B.: Stable isotopes in ecosystem studies, Ann. Rev. Ecol. Syst., 18, 293–320, 1987.

Prothman, C. and Zauner, K.-P.: Semibiotic Persistence, J. Brit. Interplanet. Soc. (JBIS), 67, 314–321, 2014.

Rasmussen, B., Blake, T. S., Fletcher, I. R., and Kilbum, M. R.: Evidence for microbial life in synsedimentary cavities from 2.75 Ga terrestrial environments, Geology, 37, 423–426, 2009.

Rikkinen, J., Grimaldi, D. A., and Schmidt, A.; Morphological stasis in the first myxomycete from the Mesozoic, and the likely role of cryptobiosis, Sci. Rep., 9.1, 19730, https://doi.org/10.1038/s41598-019-55622-9, 2019.

Roulliard, J., García-Ruiz, J.-M., Gong, J., and van Zuilen, M. A.: A morphogram for silica-witherite biomorphs and its application to microfossil identification in the early earth rock record, Geobiology, 16, 279–296, https://doi.org/10.1111/gbi.12278, 2018.

Schnittler, M. Novozhilov, Y. K., Romeralo, M., Brown, M., and Spiegel, F. W.: Fruit body-forming protists: Myxomycetes and Myxomycete-like organisms, chap. 4, 40–88, in: Syllabus of Plant Families – A, edited by: Engler, A. and Frey, W., En-

gler's Syllabus der Pflanzenfamilien Part 1/1, Stuttgart, Born-träger, ISBN: 978-3-443-01087-4, 2012.

Sergeev, V. N. and Schopf, J. W.: Taxonomy, paleoecology and biostratigraphy of the Late Neoproterozoic Chichkan microbiota of South Kazakhstan: The marine biosphere on the eve of metazoan radiation, J. Paleont., 84, 363–401, 2010.

Shourie, A. and Vijayalakshmi U.: Fungal diversity and its role in mycoremediation, Geomicrobiol. J., 39, 426–444, doi.org/10.1080/01490451.2022.2032883, 2022.

Shumlyanskyy, L., Billström, K., Hawkesworth, C., and Elming, S.-Å.: U-Pb age and Hf isotope compositions of zircons from the north-western region of the Ukranian shield: mantle melting in response to post-collision extension, Terra Nova, 24, 373–379, 2012.

Shumlyanskyy, L., Hawkesworth, C., Billström, K., Bogdanova, S., Mytrokhyn, O., Romer, R., Dhuime, B., Claesson, S., Ernst, R., Whitehouse, M., and Bilan, O.: The origin of the Palaeoproterozoic AMCG complexes in the Ukrainian Shield: new U-Pb ages and Hf isotopes in zircon, Precam. Res., 292, 216–239, 2017.

Shumlyanskyy, L., Franz, G., Glynn, S., Mytrokhyn, O., Voznyak, D., and Bilan, O.: Geochronology of granites of the western Korosten AMCG complex (Ukrainian Shield): implications for the emplacement history and origin of miarolitic pegmatites, Eur. J. Mineral., 33, 703–716, https://doi.org/10.5194/ejm-33-703-2021, 2021.

Stephenson, S. L. and Schnittler, M.: Myxomycetes, in: Archibald et al., Handbook of the protists, Springer International Publishing AG, 1–26, 2016.

Stephenson, S. L., Schnittler, M., and Nvozhilov, Y. K.: Myxomycete diversity and distribution from the fossil record to the present, Biodivers. Conserv., 17, 285–301, https://doi.org/10.1007/s10531-007-9252-9, 2008.

Struck, U.: On the use of stable nitrogen isotopes in present and past anoxic environments, in: Anoxia, evidence for eukaryote survival and paleontological strategies, edited by: Altenbach, A. V., Bernard, J. M., and Seckbach, J., Book series: Cellular origin, life in extreme habitats and astrobiology, 21, 497–513, Springer, Berlin, ISBN: 978-94-007-1895-1, e-ISBN: 978-94-007-1896-8, https://doi.org/10.1007/978-94-007-1896-8, 2012.

Tugay, T., Zhdanova, N. N., Zheltonozhsky, V., Sadovnikov, L., and Dighton, J.: The influence of ionizing radiation on spore germination and emergent hyphal growth response reactions of microfungi, Mycologia, 98, 521–527, https://doi.org/10.1080/15572536.2006.11832654, 2017.

Vasilev, A., Efimov, M., Bondarenko, G., Kozlov, V., Dzidziguri, E., and Karpacheva, G.: Thermal behavior of chitosan as a carbon material precursor under IR radiation, IOP Conf. Ser.-Mater. Sci. Eng., 693, 012002, https://doi.org/10.1088/1757-899X/693/1/012002, 2019.

Volland, J.-M., Gonzalez-Rizzo, S., Gros, O., Tyml, T., Ivanova, N., Schulz, F., Goudeau, D. Elisabeth, N. H., Nath, N., and Udway, D.: A centimeter-long bacterium with DNA contained in metabolically active, membrane-bound organelles, Science, 376, 1453–1458, https://doi.org/10.1126/science.abb3634, 2022.

Wanjun, T., Cunxin, W., and Donghua, C.: Kinetic studies on the pyrolysis of chitin and chitosan, Polym. Degrad. Stabil., 87, 389–394, 2005.

Wang, D. Y.-C., Kumar, S., and Hedges, S. B.: Divergence time estimates for the early history of animal phyla and the origin of plants, animals and fungi, P. R. Soc. Lond., 266, 163–171, 1999.

Wellman, C. H. and Strother, P. K.: The terrestrial biota prior to the origin of land plants (embryophytes): A review of the evidence, Paleontology, 58, 601–627, 2015.

Westall, F., de Witt, M. J., Dann, J., van der Gaast, S. de Ronde, C. E. J., and Gerneke, D.: Early Archean fossil bacteria and biofilms in hydrothermally-influenced sediments from the Barberton greenstone belt, South Africa, Prec. Res., 106, 93–116, 2001.

Zawadzki, J. and Kaczmarek, H.: Thermal treatment of chitosan in various conditions, Carbohydr. Polym., 80, 394–400, 2010.

Zhmur, S. I.: Origin of Cambrian fibrous kerites of the Volyn region, Lithol. Mineral Resour., 38, 55–73, 2003.